IOP Publishing and International Atomic Energy Agency Nuclear Fusion
Nucl. Fusion **47** (2007) S543–S562 doi:10.1088/0029-5515/47/10/S05

Development in the DIII-D tokamak of advanced operating scenarios and associated control techniques for ITER

M.R. Wade for the DIII-D Team

General Atomics, PO Box 85608, San Diego, CA 92186-5608, USA

E-mail: wade@fusion.gat.com

Received 3 January 2007, accepted for publication 30 April 2007
Published 17 September 2007
Online at stacks.iop.org/NF/47/S543

Abstract
Significant progress has been made on the DIII-D tokamak in the capability to control key plasma features and using such control to expand the operational limits of stationary and steady-state tokamak operation. Recent experiments have demonstrated the capability to suppress several key plasma instabilities of concern for ITER, including edge localized modes, neoclassical tearing modes and resistive wall modes. In addition, the ability to regulate the rotation and current density profiles through feedback control has been demonstrated. The use of these control techniques has allowed an expansion of the envelope of viable, stationary tokamak operation, highlighted by the demonstration of sustained ($\sim$2 s) operation of $\beta_N \simeq 4$ (50% above the no-wall stability limit) as well as fully noninductive operation with $\beta \simeq 3.5\%$. This development is supported by a vigorous basic fusion science programme, which has provided new insights into turbulence dynamics over a large range in spatial scales, new measurements of the structure of fast-ion instabilities and their effect on the fast-ion population and important information on the transport of carbon and associated tritium co-deposition on plasma facing surfaces.

PACS numbers: 52.55.Fa, 28.52.Av, 52.35.Py, 52.55.Pi, 52.55.Rk

1. Introduction

Through the development and integration of advanced control techniques and operating scenarios, the DIII-D research programme has made significant progress in its mission to develop the physics basis for the optimization of the tokamak approach to fusion energy production. This optimization requires a broad research programme capable of identifying the key underlying physics issues and methods to control them, developing and characterizing such tools and then using these tools in a synergistic manner to develop operating scenarios capable of sustained, high performance. In recent years, research on DIII-D has pioneered the development, established the feasibility and developed the physics basis for several control tools important to the success of ITER. In addition, the DIII-D Team has developed both stationary, inductive scenarios with normalized performance consistent with the $Q = 10$ baseline mission of ITER [1] and fully noninductive plasmas with normalized performance in excess of that required for the $Q = 5$ mission in ITER [1], providing additional confidence that ITER can achieve its performance objectives.

This paper presents results from DIII-D that highlight the progress made in this optimization process within the past two years. Previous overviews of the DIII-D research programme can be found in [2–4]. In section 2, examples of key control capabilities are presented including several results on instability control and internal profile control. In section 3, the present status of research aimed at providing ITER with fully characterized scenarios for both its $Q = 10$ baseline mission and $Q = 5$ steady-state mission is discussed. Finally, in section 4, examples of advances made in the basic understanding of high-temperature fusion plasmas in areas important to ITER are presented.

2. Plasma control

DIII-D is equipped with a unique set of control tools that allow precise control of key aspects of plasma stability, transport and current drive. A schematic of the various control capabilities is shown in figure 1. Many of these actuators can be used for multiple plasma control purposes, providing significant experimental flexibility. A flexible set of non-axisymmetric coils can be utilized for mitigating or suppressing both resistive

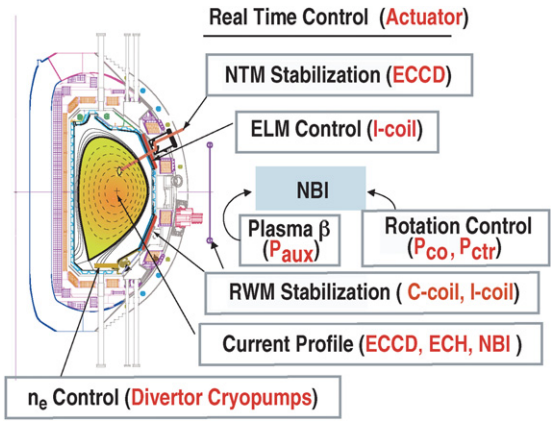

Figure 1. Poloidal cross section of DIII-D showing some of the available actuators and their primary application in plasma control.

wall modes (RWMs) and edge localized modes (ELMs) and for general error field correction. High-power, localized electron cyclotron current drive and heating (ECCD/ECH) is utilized for controlling sawteeth and neoclassical tearing modes (NTMs) as well as providing current profile control in high performance plasmas. A flexible neutral beam injection (NBI) system capable of co-, counter- and balanced neutral beam injection provides fine control of the plasma rotation. A suite of three divertor cryopumps enable excellent density control in a variety of plasma shapes, which in turn is enabled by an extensive poloidal field coil set, allowing comparative studies with other devices and detailed studies of the effect of the magnetic configuration on plasma performance. In the following sections, these actuators are first described (section 2.1) followed by a more detailed discussion of the physics enabled by these tools, including high beta instability control (section 2.2), RWM stabilization (section 2.2), ELM suppression (section 2.3), disruption mitigation (section 2.4) and profile control (section 2.5).

2.1. Control actuators

Two sets of non-axisymmetric coils (one internal to the vacuum vessel and one external to the toroidal field coils) can be used to add/reduce $n = 1, 2$ and 3 magnetic perturbations in DIII-D. The internal coil set (known as the I-coils) is a set of 12 picture-frame coils located in two arrays of six coils each above and below the outboard midplane mounted on the inner wall of the vacuum vessel with a maximum coil current of 7 kA [5]. Low latency ($\sim$50 μs) feedback control has been enabled by the recent installation of 12 high bandwidth (>40 kHz) transistor amplifiers [6]. The I-coils have been used successfully to suppress key instabilities such as ELMs and RWMs. Recent experiments have also shown that the degree of error field correction possible with the I-coils is superior to that from the external non-axisymmetric coil set [7]. The external set (known as the C-coils) was originally designed [8] for flexible error field correction [9] but has also been used extensively for $n = 1$ and $n = 3$ magnetic braking experiments as well as feedback stabilization of the $n = 1$ RWM. The C-coil consists of six picture-frame coils located at the midplane, each of which consists of four turns capable of 5 kA. These coils are generally energized by three switching-power-amplifiers (SPAs), which have a bandwidth of approximately 0.8 kHz.

The primary heating tool on DIII-D is NBI with seven separate NBI sources providing up to 17.5 MW of heating. Recently, two NBI sources were reoriented to provide $\sim$5 MW of counter-injection (i.e. applied torque is in the direction counter to the normal direction of the plasma current) [10]. With this reconfiguration, the applied torque can be maintained at very low values while injecting up to $\sim$10 MW of total NBI power. In addition, fine control of the plasma rotation is now possible, enabling experimental studies of the role of rotation in turbulence-driven transport and in certain aspects of plasma stability. Each of the neutral beam sources can be separately controlled by the DIII-D plasma control system (PCS), thereby allowing independent control of the total input power and torque. This capability has been used in a variety of experiments ranging from basic studies of the impact of rotation on confinement and stability properties (section 2.4.1) to a detailed assessment of the rotation threshold for resistive wall mode stabilization (section 2.2.2).

NBI heating is supplemented by ECCD/ECH [11]. For the experiments described here, a maximum of $\sim$2.5 MW of EC power was available, provided by five separate gyrotrons at 110 GHz. The deposition location of each gyrotron output is separately controlled by toroidally (current drive versus heating) and poloidally (radial location) steerable mirrors. While 2nd harmonic absorption is generally used, 3rd harmonic absorption has also been shown to be effective for electron heating purposes. As with the NBI systems, each of the EC systems is independently controlled by the DIII-D PCS. The EC's ability to provide localized current drive or heating enables a wide range of applications including: mitigation or suppression of limiting instabilities such as sawteeth and NTMs (section 2.2.1), off-axis current drive for controlling the current density profile in steady-state scenarios (section 3.1) and probing transport characteristics through localized heating.

DIII-D's unique ability to control density in H-mode plasmas has recently been extended to provide effective density control in high-triangularity, lower single-null (LSN) and double-null (DN) plasmas in conjunction with two existing upper divertor cryopumps, which provide density control in upper single-null (USN) plasmas. This was accomplished by modifying the lower divertor configuration so that high-triangularity plasmas could be coupled effectively to the lower divertor cryopump [12]. All of these cryopumps provide $\sim$30 $m^3\,s^{-1}$ of D_2 throughput, enabling density control in a wide range of plasma shapes and conditions (section 2.5.3).

A centralized framework for effectively utilizing these actuators is provided by the DIII-D advanced digital PCS [13], which provides a flexible environment in which to develop and implement integrated, model-based, control algorithms for these tools. Full digital architecture allows for advances in real-time processing capability (29 parallel processors presently used) and the rapid inclusion of diagnostic inputs for feedback control. Control algorithms based on physics models (e.g. modified Rutherford equation for NTM control) are now readily available and undergoing continuous refinement [14]. In addition, automated shutdown algorithms are in use to avoid NTM-induced disruptions in high performance plasmas. The real-time information available

to the PCS for use in these control algorithms continues to expand. For example, equilibrium reconstructions including internal magnetic measurements using the motional Stark effect (MSE) diagnostic [15] are available every 4–8 ms, depending on the required accuracy for the application. Radial profiles of the ion temperature and plasma rotation from spectral analysis of charge-exchange recombination (CER) spectroscopy measurements are also available in real-time [16]. When processing the eight chords now included in the PCS, toroidal rotation measurements are available every 10 ms, providing adequate sampling for precise, timely control. Comparisons of this real-time CER analysis with standard analysis techniques show extremely good agreement.

2.2. High β instability control

Because of the strong dependence of fusion power on the achievable plasma pressure ($P_{\rm fus} \propto \beta^2$ at constant toroidal field), high β operation is a prerequisite for high fusion gain and economical fusion power production. Operating at sufficiently high β in ITER or any other fusion device to achieve its fusion gain goals will require the capability to avoid or suppress magnetohydrodynamic (MHD) instabilities that limit the attainable pressure. Of utmost concern for ITER are NTMs, which are predicted to limit the attainable β in the ITER baseline ($Q = 10$) scenario, and RWMs, which are predicted to limit the attainable β in the ITER steady-state ($Q = 5$) scenario. Recent experiments on DIII-D have demonstrated the capability to suppress each of these key instabilities by external means. Furthermore, such suppression has allowed sustained operation at significantly higher β values than would be possible without suppression. In the best cases, the ideal stability limit is approached with $\beta_{\rm N} \sim 4$ sustained for nearly 2 s. Here, ($\beta_{\rm N} = \beta/I_{\rm p}/aB_{\rm T}$) where $\beta = 2\mu_0\langle p\rangle/B_{\rm T}^2$, $\langle p\rangle$ is the volume-averaged kinetic pressure, $I_{\rm p}$ is the plasma current, a is the plasma minor radius and $B_{\rm T}$ is the toroidal magnetic field.

2.2.1. Suppression of neoclassical tearing modes. The $m = 2/n = 1$ NTM is expected to be the most significant instability limiting the attainable β in the ITER baseline ($Q = 10$) scenario [1]. In addition, there is a significant risk of such an instability leading to a disruption. Hence, a means to suppress and/or control this instability is essential for the success of ITER. Previous experiments on DIII-D have demonstrated the efficacy of using highly localized ECCD at the $q = 2$ surface to stabilize the $m = 2/n = 1$ NTM [17]. Recent experiments (figure 2) have shown that once the NTM is stabilized, the plasma pressure can be increased and then maintained at the free-boundary stability limit, provided the ECCD is applied locally to the $q = 2$ surface [18]. Various control algorithms have been developed and tested to maintain the ECCD deposition location optimally positioned to provide sufficient current-drive in the NTM island region. In this case, a 'search-and-suppress' algorithm is initially used to provide the proper alignment. This algorithm adjusts the $q = 2$ location (through dynamic changes in the toroidal field $B_{\rm T}$) in a stepwise fashion until the optimum location for NTM suppression is found based on the tearing mode amplitude determined from external magnetic probes [19]. Once the NTM is suppressed,

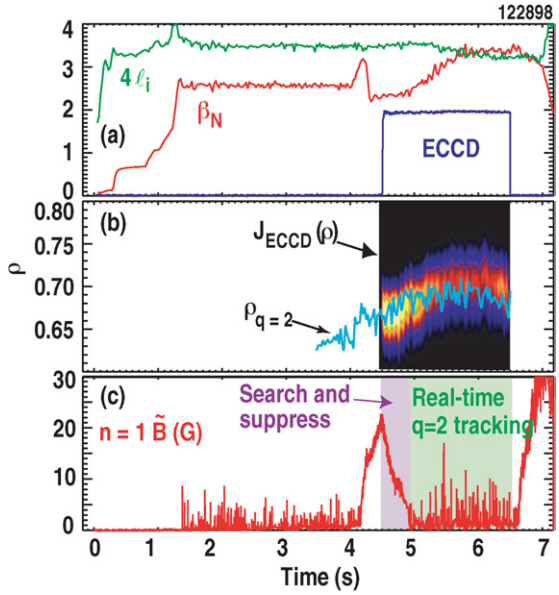

Figure 2. Temporal evolution of a discharge in which ECCD is utilized to stabilize the $m = 2/n = 1$ NTM as plasma pressure is increased to the no-wall β limit. Shown are (a) $\beta_{\rm N}$ (red), the approximate no-wall ideal kink mode β limit ~4 $l_{\rm i}$ (green), and the ECCD power (blue), (b) contour plot of $J_{\rm ECCD}(\rho, t)$ computed by TORAY-GA and the location of the $q = 2$ surface (cyan) and (c) amplitude of $n = 1$ magnetic fluctuations measured at the wall. Colour scale for $J_{\rm ECCD}(\rho, t)$ in (b) is: black—0 MA m^{-2}, blue–0.04 MA m^{-2}, red—0.08 MA m^{-2}, yellow—0.12 MA m^{-2}, white—0.16 MA m^{-2}.

tracking of the $q = 2$ surface based on real-time equilibrium reconstructions is used to maintain good alignment between the ECCD deposition and the $q = 2$ surface. Previous experiments have shown that accurate tracking of this $q = 2$ surface is important during the programmemed β increase following suppression as the associated Shafranov shift causes the location of the $q = 2$ surface to move slightly [20]. Using these algorithms, optimal alignment of the ECCD deposition region with the $q = 2$ surface is maintained throughout the ECCD phase. With the NTM effectively suppressed, $\beta_{\rm N}$ is increased and maintained for ~1 s at the no-wall, ideal stability limit ($\beta_{\rm N} \sim 3.2$). Due to the launching geometry in this case, calculations indicate that considerable EC power is absorbed at the third harmonic resonance with only 40% of the launched ECCD power of 2.4 MW absorbed at the 2nd harmonic. Through active tracking of the $q = 2$ surface, the ECCD deposition location and the corresponding current-drive location is maintained within $\Delta\rho = 0.02$ or approximately 1.5 cm of the $q = 2$ surface throughout the entire ECCD phase as is shown in figure 2(b). This absorbed power drives a total current of approximately 16 kA with a peak current density of 12.2 A cm^{-2}, compared with a local bootstrap current density of 17.1 A cm^{-2} and an equilibrium current density of 75 A cm^{-2}. About 100 ms after the ECCD is turned off at 6.5 s, a new $m = 2/n = 1$ NTM is triggered, confirming the role of the ECCD in the suppressing of the NTM. Separate experiments on DIII-D have demonstrated the capability to preemptively suppress the $m = 2/n = 1$ NTM even as $\beta_{\rm N}$ is increased and maintained for ~1 s at the no-wall, ideal stability limit. In this case, real-time equilibrium reconstructions are used throughout the ECCD phase to maintain proper alignment

between the ECCD deposition location and the $q = 2$ surface. The ECCD power threshold to achieve pre-emptive suppression has not yet been explored though results from JT-60U [21] suggest that the required power is substantially less than that required for suppression once the NTM has been triggered.

The NTM suppression capability demonstrated in this case is enhanced by use of an off-line control design process that uses the physics embodied in the modified Rutherford equation (MRE) to simulate NTM suppression in representative DIII-D discharges to determine the proper settings for important parameters in the control algorithm [19]. These parameters include the time constants for the search process as well as thresholds for NTM size and suppression rate that determine control algorithm dynamics. While the MRE is not used directly in the real-time control, it is used not only in initial design development but also in simulations to confirm algorithm performance.

2.2.2. Resistive wall mode stabilization. Success in achieving the second primary physics objective of ITER—steady-state, $Q = 5$ operation—is expected to require β values in excess of the no-wall, ideal stability limit $\beta^{\text{no-wall}}$. Access to these β levels requires the ability to stabilize RWMs, which are destabilized as β is increased above $\beta^{\text{no-wall}}$ [22]. Two methods of RWM stabilization have been demonstrated on DIII-D and other devices in recent years: rotational stabilization in which the plasma rotation (or associated rotational shear) is sufficient to stabilize the RWM [23–30] and direct feedback stabilization using non-axisymmetric control coils to suppress the growth of the RWM [31, 32].

In the rotational stabilization case, previous studies from DIII-D indicated that plasma rotation is highly effective in stabilizing RWMs, provided a moderate rotation velocity (typically 1–2% of the Alfvén velocity) is maintained at the $q = 2$ surface [33]. In these previous experiments, the threshold velocity for stabilization was determined by slowly decreasing the plasma rotation using magnetic braking until the RWM was destabilized. In recent experiments in which NBI torque was varied to reduce the plasma rotation, the measured threshold for destabilizing the RWM is considerably lower [34]. The ability to operate above $\beta^{\text{no-wall}}$ for $\sim$1 s at very low-rotation values is exemplified in figure 3, where rotation values in the outer part of the plasma remain below 0.5% of the Alfvén velocity for more than 1 s. The stable rotation profile (figure 3(*c*)) is well below the rotation profile in which the RWM was destabilized in a similar discharge with magnetic braking. The larger data set from DIII-D is supportive of this lower threshold. Shown in figure 4 is the measured critical velocity for RWM stabilization at the $q = 2$ surface normalized to the Alfvén velocity as a function of $C_\beta = (\beta - \beta^{\text{no-wall}})/(\beta^{\text{ideal wall}} - \beta^{\text{no-wall}})$. Over a wide range of C_β, the measured critical velocity is less than 0.5% of the Alfvén velocity in the cases using balanced torque for rotation control while the threshold is >1% for the cases using magnetic braking. The results shown here incorporate recently developed corrections for atomic physics effects, including the energy dependence of the charge-exchange cross section

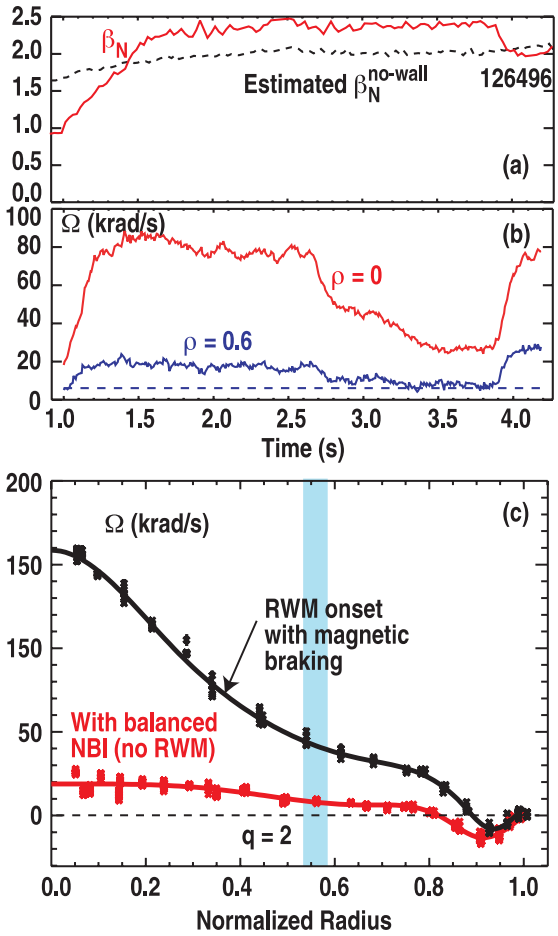

Figure 3. (*a*) DIII-D discharge demonstrating sustained operation above the no-wall β limit (2.4 l_i) at (*b*) very low rotation. (*c*) (black) Toroidal rotation profile at RWM onset when using magnetic braking; (red) stable rotation profile when using NBI torque control for rotation control with no magnetic braking applied. The dashed line in (*b*) represents 0.5% of the Alfven velocity at the $q = 2$ surface, comparable to the expected rotation in ITER.

and contributions from excited beam neutrals [35]. In low-torque plasmas, these corrections can be of the same order of magnitude as the measured rotation. However, the accuracy of the correction for the cross section energy dependence is improved by the fact that this diagnostic now views both co- and counter-injected neutral beams, in which the correction has opposite signs.

While a complete understanding of the differences in the observed rotational threshold for RWM stabilization is still in progress, analysis suggests that the nonlinear interaction between the plasma rotation and resonant amplification of the fields used for magnetic braking may be responsible for the higher threshold previously seen with magnetic braking [36, 37]. In particular, the observed threshold velocity with magnetic braking is approximately 1/2 of the unperturbed (i.e. before applying magnetic braking) rotation velocity, which is consistent with predictions from the 'induction motor' model of error field-driven reconnection [38, 39] and a conceptually similar process proposed involving the resistive wall mode [40].

Calculations of the MHD stability using MARS-F [41] for these low-rotation cases with NBI torque control indicate

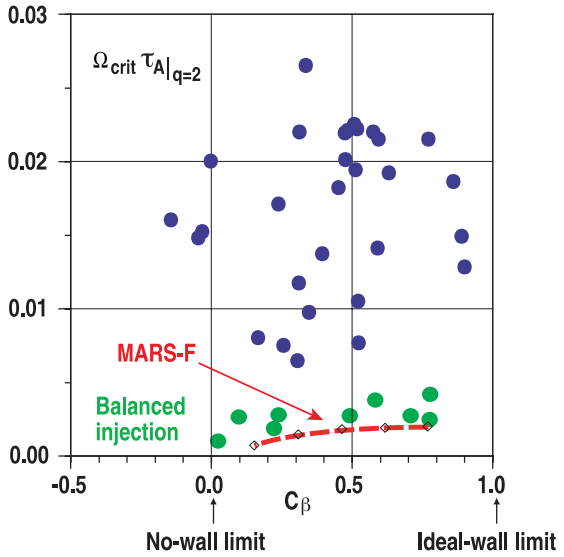

Figure 4. Critical rotation for RWM stabilization normalized to the Alfvén velocity versus C_β for cases using magnetic braking (blue) and NBI torque variation (green) for rotation control. The theoretical prediction of the rotation threshold from the MARS code using the kinetic damping model is shown as the red curve.

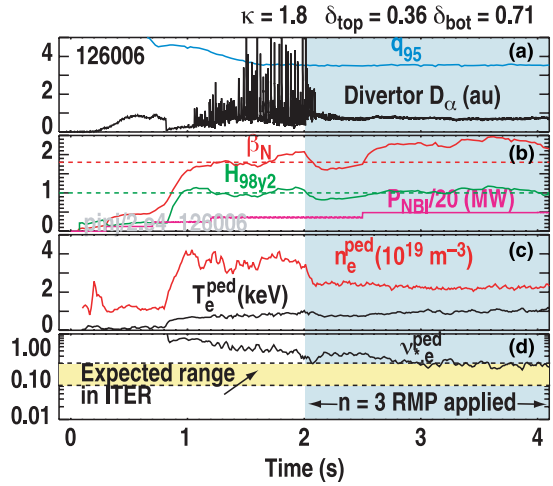

Figure 5. Complete ELM suppression using $n = 3$ RMP in a discharge with a shape and collisionality similar to that in ITER. Shown are (*a*) q_{95} (cyan) and divertor D_α signal (black), (*b*) β_N (green) and H_{98y2} (red) and the NBI power (magenta), (*c*) the pedestal electron density (red) and temperature (black) and the electron pedestal collisionality (black) and applied $n = 3$ perturbation timing (green). The dashed lines in (*b*) represent the ITER $Q = 10$ baseline target values for β_N and H_{98y2}.

that the measured experimental rotation profile (of the carbon impurity ions) is generally sufficient to stabilize the plasma up to the ideal wall limit when the kinetic damping model is used (figure 4). While these calculations suggest that the kinetic model for RWM damping may be adequate in making extrapolations to ITER, further studies are necessary to resolve several issues including the adequacy of using the carbon rotation velocity in the stability calculations, the key aspects of the rotation profile in determining the stability and the impact of existing error fields on RWM stability. In particular, the similarities of the rotation profile in the edge region in figure 3(*c*) suggest a possible role of edge rotation on RWM stability.

Separate studies have shown that even in the presence of high rotation, transient events such as ELMs can cause a rapid decrease in the edge rotation leading to RWM destabilization. In such cases, the use of internal coils (I-coils) powered by high bandwidth audio amplifiers for fast RWM feedback control has been shown to be effective in suppressing RWM growth and allowing robust high β operation. Through combined rotational and feedback stabilization, sustained operation at very high β has been demonstrated (section 3.1).

2.3. ELM suppression

The control of ELMs is a serious concern for ITER due to potentially unacceptable levels of erosion of the plasma facing components due to the repetitive, high-power fluxes associated with the ELMS. Such a control technique must be compatible with maintaining a high pedestal pressure due to the strong dependence of fusion gain on the edge plasma pressure. A potential solution to this issue has emerged from experiments on DIII-D that utilize edge resonant magnetic perturbations (RMPs) with $n = 3$ symmetry to completely eliminate ELMs [42]. Recent experiments have extended this capability to include complete ELM suppression in a plasma shape similar to the ITER baseline shape (elongation $\kappa = 1.8$, upper triangularity $\delta_{top} = 0.36$, and lower triangularity $\delta_{bot} = 0.71$) and at a pedestal collisionality $\nu_{*e}^{ped} \approx 0.2$ comparable to that anticipated in ITER [43]. This capability is shown in figure 5. The application of an $n = 3$ RMP at 2.0 s results in the immediate elimination of ELMs even as good confinement quality relative to the standard ELMing H-mode scaling H_{98y2} [44] and moderate β operation are maintained. The ability to suppress ELMs reliably has been found to be highly sensitive to plasma shape and q_{95} and systematically improves with lower density, higher input power and larger $n = 3$ RMP amplitude [43]. Transport and stability analysis has shown that the observed ELM suppression results from changes in edge particle transport such that the operational point with the $n = 3$ RMP activated is slightly below the peeling–ballooning stability limit [45, 46]. This increase in particle transport is correlated with a narrowing of the radial electric field E_r well in the edge and an increase in density fluctuations as measured by FIR scattering in the edge region [47]. The narrowing of the E_r well results in a smaller region of high $E_r \times B$ velocity shear and hence a reduced region of turbulence suppression in the edge region, key components of the formation of the edge transport barrier in H-mode plasmas [48]. The measured fluctuations are broadband in nature, which is distinct from the coherent structure that is typically observed in QH-mode plasmas [49].

The degree of ELM suppression shown in figure 5 is only observed when the perturbation spectrum of the I-coil (determined by its geometry and wiring configuration) has a strong harmonic that is resonant with field line topology in the edge region. Due to the geometry and chosen wiring configuration of the I-coil set for this experiment, the largest harmonic of the applied field in the pedestal region is that of $m = 11/n = 3$, generating a large island region at the $q = 11/3$ surface that overlaps with lesser $n = 3$ harmonics

to generate a stochastic magnetic structure in the edge region. This leads to a fairly narrow window near $q_{95} \sim 3.7$ to achieve full ELM suppression. This is somewhat higher than the ITER baseline design of $q_{95} \sim 3.0$. However, conceptual designs of non-axisymmetric coils for ITER [50] suggest that an appropriate harmonic spectrum can be generated that maximizes the perturbation in the pedestal region with minimal impact on the core plasma.

2.4. Disruption mitigation

While stabilization of the RWMs and NTMs will reduce the number of full-current disruptions in ITER, some unplanned plasma terminations will likely still occur, requiring a robust system for mitigating the effects of such a disruption. DIII-D pioneered the use of massive gas injection (MGI) to reduce the impact of excessive thermal loads, halo currents and runaway electron generation resulting from unmitigated plasma disruptions [51] and is now in the process of developing the physics basis of this technique. Recent studies of the mitigation process suggest that the transport of the impurities introduced by MGI is a multi-stage process in which radial transport of the impurities from a succession of MHD reconnection events is an essential component [52]. These studies have shown conclusively that the injected impurities are ionized very near the plasma surface over a wide range of conditions, consistent with the expectations of theory and indicative that processes other than direct neutral penetration must be responsible for the rapid, inward transport of the impurities. Detailed analysis of the data from a systematic scan of the $q = 2$ depth within the plasma (using a simple scan of q_{95}) shows the onset of the central temperature collapse following MGI of argon is increasingly delayed as the $q = 2$ depth is increased. Furthermore, an increase in the duration of the current quench is observed with the amplitude of the current channel spreading at the start of the current quench consistent with field line ergodization inside the $q = 2$ surface. Preliminary experiments have been conducted with a new valve with gas throughput rates up to 25 times larger than the valve used for previous experiments in hopes of demonstrating the capability of reaching the so-called Rosenbluth density, above which Coulomb amplification is predicted to be quenched [53].

2.5. Control of plasma profiles

In ITER, control of the plasma density, current density and rotation profiles will take on added importance due to the demonstrated dependence of transport and stability on these profiles and the inability to use external means to control the temperature profiles directly due to large self-heating by the alpha particle population. The ability to control each of these profiles has been demonstrated on DIII-D. Examples of the present capabilities with regard to rotation, current and density profile control are presented in this section.

2.5.1. Rotation control. Plasma rotation is predicted to have important effects on both the transport and the stability of tokamak plasmas, making control of rotation a high leverage tool in achieving optimum performance. Tests of these theories to date have been limited due to the inability to control

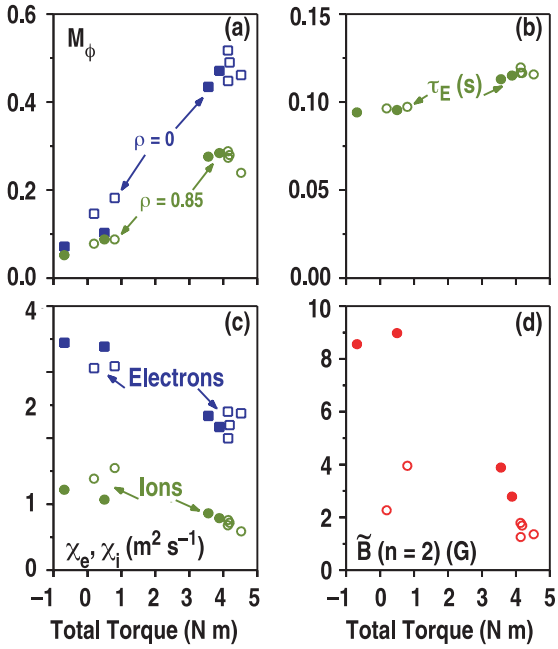

Figure 6. Measured variation of (*a*) core and edge Mach number, (*b*) energy confinement time, (*c*) ion and electron thermal diffusivity at $r/a = 0.5$ and (*d*) $m = 3/n = 2$ NTM amplitude with torque input in $q_{95} = 4.5$ (open) and $q_{95} = 4.0$ (closed) hybrid plasmas.

the torque input (and the resulting rotation) precisely. To provide the ability to control rotation in DIII-D, the neutral beam system on DIII-D has been recently reconfigured to provide up to 5 MW of counter-NBI injected power along with 12.5 MW of co-NBI injected power, thereby providing a powerful tool for controlling plasma rotation [54]. The impact on transport and MHD activity in the hybrid regime [55] is illustrated in figure 6, which shows the variation in the Mach number, energy confinement, ion and electron thermal diffusivity (χ_i and χ_e) at $\rho = 0.5$, and the $m = 3/n = 2$ NTM amplitude activity during a systematic scan of the torque input. The Mach number here is defined as $M_\phi = v_\phi/C_s = v_\phi(m_D/2eT_e)^{1/2}$ where v_ϕ is the measured toroidal rotation, m_D is the deuteron mass, and T_e is the measured electron temperature. Data from scans at $q_{95} = 4.5$ (open symbols) and $q_{95} = 4.0$ (closed symbols) are included. In all these cases, the plasma density $= 4.5 \times 10^{19}$ m^{-3} and $\beta_N = 2.6$ are maintained constant, resulting in an approximately pure scan of Mach number with other dimensionless quantities held fixed. As expected, the rotation velocity (or Mach number) increases as the torque input is increased. More importantly, the rotational shear (or equivalently the $E \times B$ shear) also increases strongly as the torque is increased. This strong increase in the $E \times B$ shear is accompanied by an increase in the global energy confinement time and decreases in both χ_i and χ_e. GLF23 [56] analysis of cases near the extremes of the torque variation in figure 6 indicate that $E \times B$ shear is important in reproducing the measured T_i profiles in the co-injection case while it plays only a minor role with more balanced injection (figure 7). The GLF23 model uses a set of gyro-Landau fluid equations that include kinetic effects such as gyro-averaging and Landau damping. The model in this case uses the measured density, current and toroidal rotation profiles and self-consistently computes the ion and

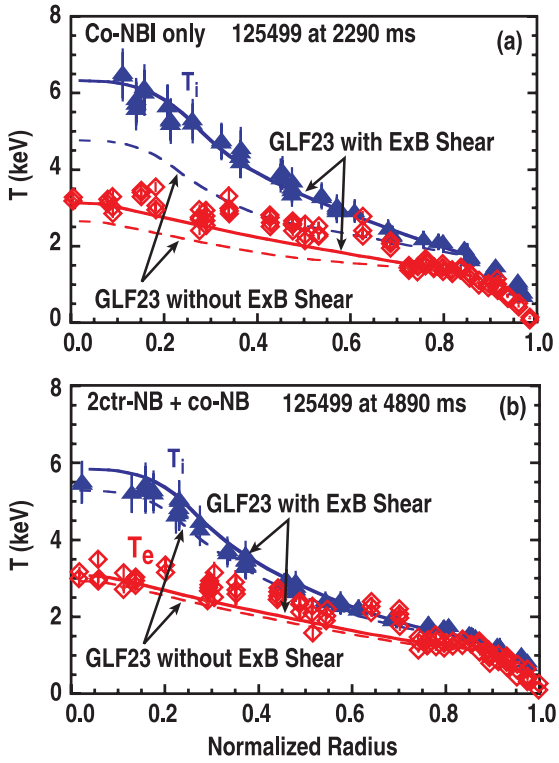

Figure 7. Comparison of experimental ion (blue triangles) and electron (red diamonds) temperature profiles with predictions using the GLF23 model with (solid) and without (dashed) $E \times B$ shear. Panel (a) shows the calculation for a time with pure co-injection and panel (b) shows the calculation for a time with more balanced injection.

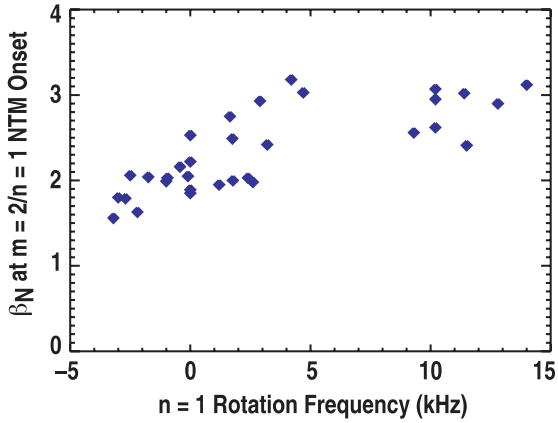

Figure 8. Pressure at which an $m = 2/n = 1$ tearing mode occurred versus the rotation frequency of the mode at onset (kHz). Discharges are conventional H-mode at $q_{95} = 4.5$ with sawteeth.

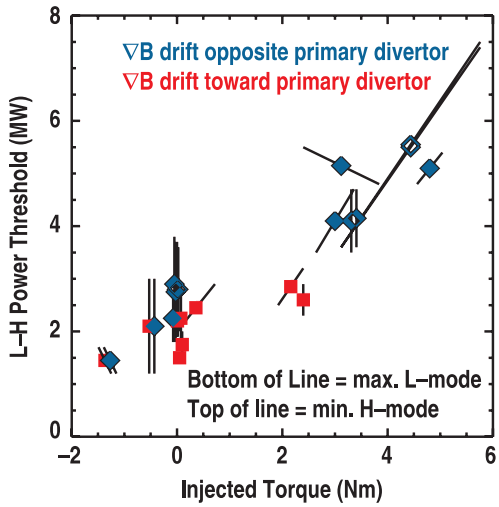

Figure 9. L–H power threshold (MW) versus external torque input (N m) for ion ∇B drift toward (square) and away (diamond) from the primary divertor. The bottom of the lines on the plot indicates the highest power case in the power ramp that remained in L-mode. The top of the lines on the plot indicates the power and torque of the next step, which caused H-mode. A vertical line indicates the power was increased with no change in torque; a slanted line indicates both power and torque changed.

electron temperature profiles. Agreement with the measured T_e profiles is not generally as good as that of T_i, but preliminary assessments indicate that the TGLF transport model (currently under development) [57] will be more accurate in reproducing the measured T_e profiles.

One of the interesting observations from figure 6 is that as the external torque (or rotation velocity) increases, the amplitude of the $m = 3/n = 2$ NTM typically seen in hybrid plasmas decreases, especially in the $q_{95} = 4.5$ case. In separate experiments, the onset beta threshold for $m = 2/n = 1$ NTMs has been shown to be quite sensitive to plasma rotation. A 50% increase in the onset β_N is observed as the plasma rotation is varied from -5 to 5 kHz (figure 8), where the positive frequency is co-rotation as in the sign convention for the torque. Above 5 kHz, there appears to be little increase in the β_N at which the mode appears. Tests of the possible effects of intrinsic $n = 1$ error fields indicate that the effect on the onset β_N limit is smaller than the variation seen in figure 8. This observation in conjunction with the asymmetric response around zero rotation frequency indicate static error fields are not playing a significant role in the observed trend. In these cases, the total current driven by the NBI is small, suggesting that its influence on the current profile will be small. Nevertheless, the effect of even these small changes on the classical tearing stability index (Δ') may be important but has not yet been quantified.

The effect of torque input on the L–H transition power threshold $P_{L\to H}$ has also been assessed using small changes in the injected power at various torque input levels. These experiments show a striking variation in $P_{L\to H}$ with the external torque as is shown in figure 9. Across the range in external torque, a factor of 3 variation in $P_{L\to H}$ is observed. At low external torque input, little difference is observed in $P_{L\to H}$ as the plasma shape is changed from having the ion grad-B drift toward or away from the primary divertor (i.e. the divertor whose X-point defines the primary separatrix of the core plasma). At higher injected torque, the data suggests a possible difference in $P_{L\to H}$ as the ion grad-B drift direction is varied but is inconclusive in this respect. Note, however, that in previous cases with co-injection only (i.e. high input torque), a factor of 2 difference in $P_{L\to H}$ was observed with $P_{L\to H}$ lower in the case with the ion grad-B drift in the direction of the primary divertor [58]. These new observations suggest that (1) $P_{L\to H}$ is quite sensitive to the applied torque and/or associated rotation and (2) the previously observed large difference in

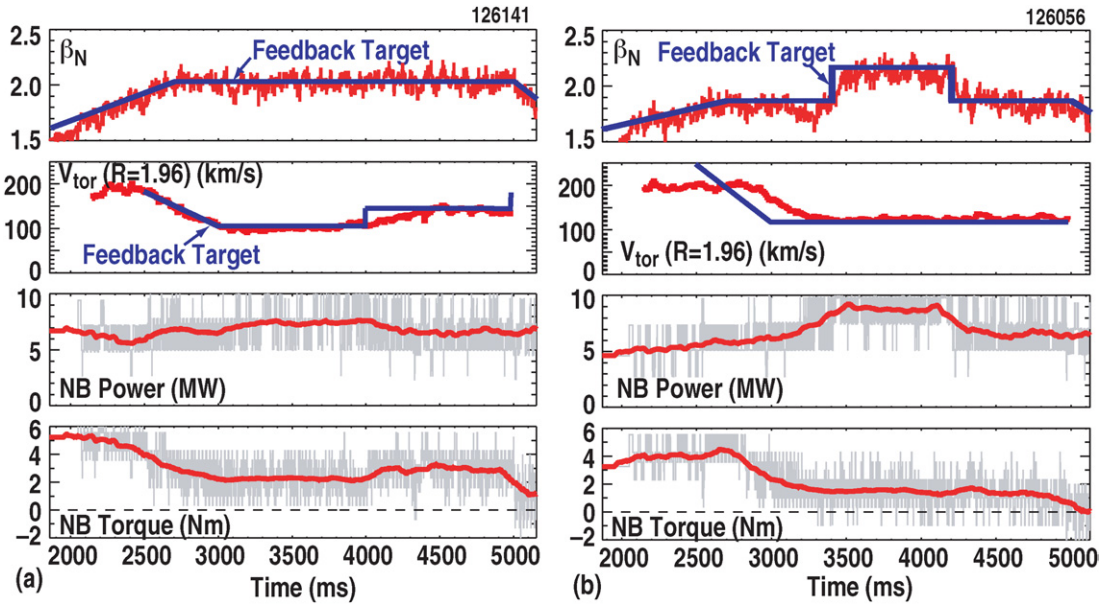

Figure 10. Demonstration of independent feedback control of stored energy and toroidal rotation. (*a*) Stored energy constant, toroidal rotation changed. (*b*) Stored energy changed, toroidal rotation constant. The gray traces in the NB power and torque are the actual signals while the red traces are smoothed with a 200 ms moving average to elucidate the trends.

$P_{L\to H}$ with ion grad-B drift direction may be due to the high level of input torque used in these cases. More studies are necessary to determine if the observed trends are a rotational effect (due to the applied torque) or associated with changes to the radial electric field (due to direct ion loss).

Utilizing the capability to separately control the total input power and torque input via NBI, independent feedback control of toroidal rotation and β has been developed and demonstrated. Figure 10 shows two examples of this. In the example on the left, the stored energy is held constant after 2.7 s, while the rotation request has a step increase at 4 s. As expected the torque required increases. The power required to maintain fixed stored energy decreases, consistent with an improvement in confinement with rotation as seen in figure 6. In the example on the right, the stored energy request is increased at 3.4 s, while the rotation request is constant.

2.5.2. Current density profile control. Active control of the current density profile $J(\rho)$ (or equivalently the safety factor q profile) offers many advantages. Both drift wave turbulence and ballooning instabilities are sensitive to magnetic shear, generally improving at either negative (or very low) magnetic shear [$s = (r/q)\,\mathrm{d}q/\mathrm{d}r < 0.5$] or high magnetic shear ($s > 1.5$). In addition, the effect of a perfectly conducting wall (or methods that mimic the role of such a wall) on stabilizing low-n kink modes improves substantially as $J(\rho)$ is broadened, providing the means to operate at very high β. The capability to actively control key aspects of the q profile evolution in a regulated fashion during the target development phase of a high β plasma has been demonstrated in recent experiments using the DIII-D PCS [59]. These studies have shown that the most effective means for controlling the q profile evolution during this early portion of the discharge is through plasma heating to modify the conductivity profile and that ECH and NBI heating are equally effective as actuators.

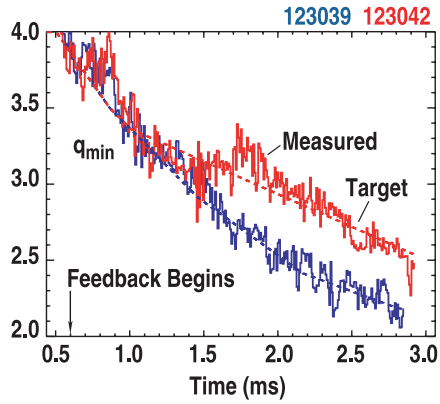

Figure 11. Two cases demonstrating the capability to regulate the evolution of q_{min} through feedback control of the neutral beam input power using the DIII-D PCS. The target q_{min} in each case is shown as the dashed line with the solid lines representing the real-time measurement of q_{min}.

This capability is illustrated in figure 11, which shows the measured and target values of q_{min} in two separate cases in which neutral beam heating was actively controlled to maintain q_{min} at relatively high values ($q_{min} > 2$) over a long duration (~2 s). Closed loop feedback control here is enabled by the aforementioned capability to do real-time equilibrium reconstruction including the MSE measurements. The values of $q(0)$ and q_{min} determined from this real-time analysis are nearly identical to those obtained from off-line analysis using EFIT. This capability has been used to tailor the target q profile in advanced scenario development (figure 17 in section 3.1). Work is now in progress to improve the control model from a simple proportional gain controller as is used in figure 11 to one that has a physics-based model for the response of the plasma to application of the ECH or NBI heating, thereby allowing separate control of q_{min} and $q(0)$.

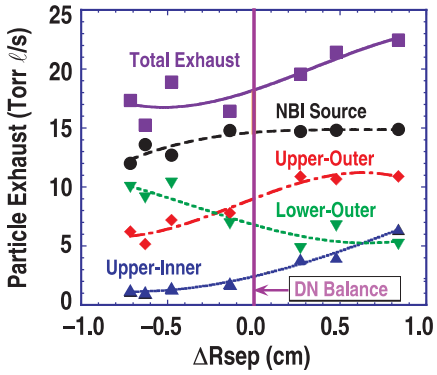

Figure 12. Measured variation with magnetic balance of the particle exhaust rates of the upper-outer (red diamonds), upper-inner (blue triangles) and lower-outer (green inverted triangles) divertor cryopumps, the beam fuelling rate (black circles) and total exhaust rate (blue squares) in long-pulse, moderate performance discharges. ΔR_{sep} represents the distance at the midplane between the flux surfaces connecting to the upper and lower X-points.

2.5.3. Density control Plasma density controls many aspects of fusion plasma operation through direct processes such as fusion power density ($P_{fus} \propto n^2$ at constant temperature) but also through indirect means such as noninductive current-drive efficiency, divertor detachment, etc. Detailed studies assessing the relative contribution of the three divertor cryopumps to the overall density control as well as experiments utilizing this new capability for density control in DN plasmas have been carried out. In a series of long-pulse, moderate performance ($\beta_N = 2.5$, $H_{89} = 2.2$), moderate density ($n_e = 5 \times 10^{19}$ m^{-3}, $n_e/n_{GW} = 0.5$) discharges, the exhaust throughput of each pump was measured as the magnetic balance is varied from USN through DN to LSN. The results are shown in figure 12. Here, the magnetic balance is parameterized in terms of ΔR_{sep}, which is the distance at the midplane between the flux surfaces connecting to the upper and lower X-points. By convention, $\Delta R_{sep} > 0$ is USN and $\Delta R_{sep} < 0$ is LSN. Evident from figure 12 is that the relative contribution of each pump changes significantly as ΔR_{sep} is varied with the primary exhaust coming from the outer leg of the primary divertor. Nevertheless, over the entire range in ΔR_{sep}, the total particle exhaust exceeds the particle input from NBI. Hence, in all of these cases, divertor exhaust is not only providing full exhaust of the NBI particle sources but also reducing the net wall inventory of particles.

A primary motivation for the modification of the lower divertor was to provide density control for good current-drive efficiency in high-triangularity DN plasmas capable of high beta. The progress provided by this modification is depicted in figure 13. In previous experiments [60] using a high-triangularity DN plasma shape (green traces in figure 13) but without lower divertor pumping, sustained operation near $\beta_N = 4$ was obtained but accompanied by an uncontrolled increase in density resulting in either very poor EC wave absorption due to refraction or low ECCD efficiency. In subsequent experiments [61], using a high triangularity, USN plasma shape (red traces in figure 13), adequate density control was obtained to achieve good ECCD efficiency but performance was limited to $\beta_N < 3.5$ due to reduction in plasma shaping necessary to obtain adequate particle exhaust.

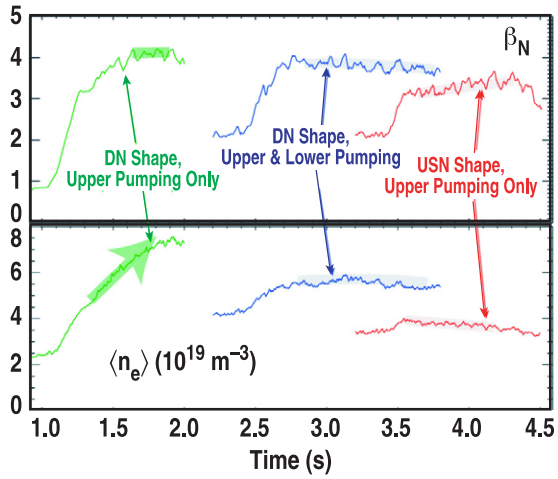

Figure 13. Temporal evolution of β_N (top panel) and plasma density (bottom) for discharges with (green) a DN shape with upper divertor pumping but no lower divertor pumping, (red) a USN shape with upper divertor pumping and (blue) a DN shape with both upper and lower divertor pumping.

In recent experiments using both upper pumps and modified lower divertor (blue traces in figure 13) sustained operation with $\beta_N \sim 4$ is again achieved in the high-triangularity DN plasma shape but with much better density control than in the 2002 experiments. While the differences in density control in the new experiments (blue) relative to the 2002 cases may be partly attributable to differences in the target plasmas in the two cases, direct comparisons between the old and the new divertor configurations have shown improved density control with the new lower divertor configuration. The optimization of density control with the favourable DN shape and the new lower divertor has not been completed, and it is anticipated that through this optimization density levels comparable to those from the 2004 USN experiments can be routinely achieved.

3. Advanced scenario development for ITER

A major long-term goal of the DIII-D research programme is the development and characterization of robust, advanced operating scenarios that can supplant the conventional, inductively-driven, ELMing H-mode plasma as the benchmark in tokamak performance. Towards this goal, the integration of the control techniques described in section 2 has enabled an expansion of the envelope of viable, stationary tokamak operation in DIII-D, providing confidence that ITER can achieve (and potentially exceed) its basic research mission tasks and increasing the credibility of high β, steady-state, tokamak operation. In addition, the successful integration of these tools has allowed tests of the compatibility of these enhanced performance regimes with anticipated conditions in burning plasmas, such as low rotation, $T_e \approx T_i$, and high radiative power fractions.

3.1. High β, steady-state scenarios

The credibility of high β, steady-state, tokamak operation and the ability to achieve $Q = 5$ steady-state operation in ITER has been bolstered by recent experiments in DIII-D

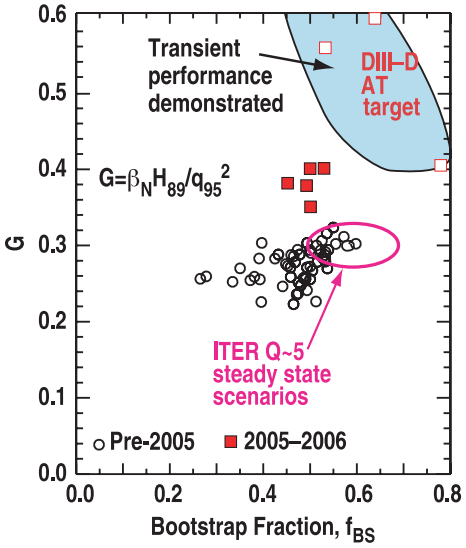

Figure 14. Achieved values of G and f_{bs} in DIII-D discharges. The open squares in the shaded region represent discharges using B_T and I_p ramps to transiently achieve high performance while the closed squares use techniques that are in principle capable of steady-state operation. The open circles are from data prior to the 2005 experimental campaign.

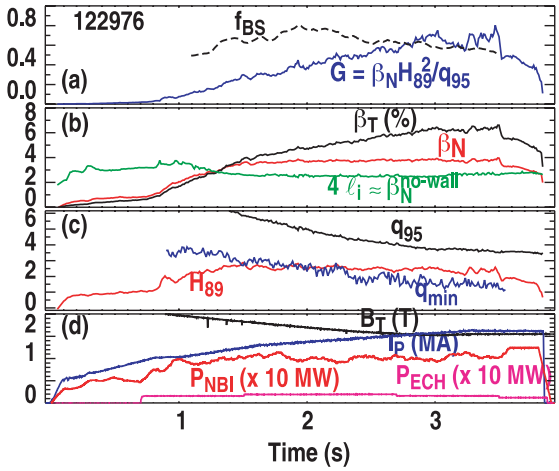

Figure 15. Temporal evolution of a discharge with $\beta_N > 3.8$ sustained for over 2 s in which simultaneous B_T and I_p ramps along with off-axis ECCD are used to form and maintain a broad current density profile. Shown are (*a*) $G = \beta_N H_{89}/q_{95}^2$ (blue) bootstrap current fraction f_{bs} (black dashed), (*b*) toroidal beta β_T (black), normalized beta β_N (red) and an estimate of the no-wall beta limit $\sim 4\, l_i$ (green), (*c*) minimum (blue) and edge safety factor q_{95} (black) and confinement quality H_{89} and (*d*) toroidal field B_T (black), plasma current I_p (blue), neutral beam (red) and ECH (magenta) power.

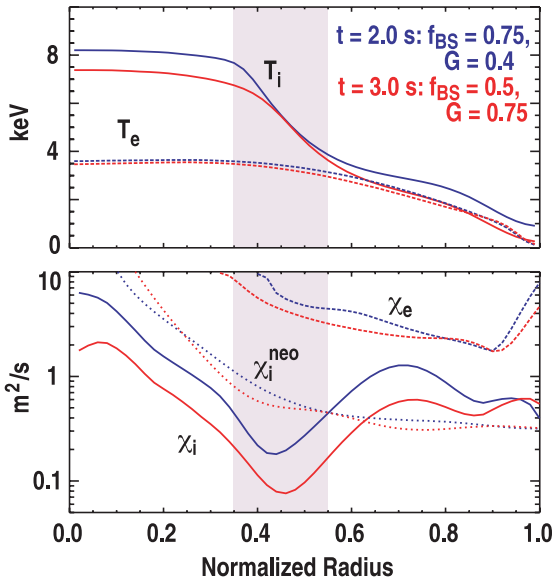

Figure 16. (*a*) Fitted profiles of ion and electron temperature and (*b*) inferred ion and electron thermal diffusivities at the beginning and end of the high performance phase of figure 15. The ion neoclassical thermal diffusivity is shown as the dashed line in (*b*).

demonstrating sustained ($\sim$2 s) operation with $\beta_N \sim 4$ (50% above the no-wall stability limit) as well as fully noninductive operation with $\beta \sim 3.5\%$. The progress made in 2005–2006 is illustrated in figure 14 where the fusion gain figure of merit $G = \beta_N H_{89}/q_{95}^2$ (where H_{89} is the confinement quality relative to the L-mode confinement scaling [62]) is plotted versus the bootstrap current fraction $f_{bs} = I_{bs}/I_p$. In 2004, proof-of-principle, advanced tokamak discharges had been developed that marginally met the ITER steady-state scenario target values ($G = 0.3$, $f_{bs} = 50\%$) [61]. Over the past two years, higher performance discharges ($G = 0.4$, $f_{bs} = 55\%$) have been developed based on the successful integration of several of the aforementioned control tools (e.g. RWM stabilization, current profile control, density control). Insufficient ECCD power to maintain the current density profile during the high β phase has limited efforts to extend these to fully noninductive operation.

The 2005–06 data points in figure 14 include two separate lines of research in which the target q profiles are obtained by distinctly different means. In both cases, highly shaped (elongation $\kappa = 1.9$, triangularity $\delta = 0.65$), balanced DN plasma shapes are utilized to maximize the attainable β. The first class of discharges utilizes feedback control of T_e and n_e during the target formation phase along with simultaneous ramps of I_p and B_T to produce broad current profiles with moderate, negative central shear (NCS) and $q_{min} > 2$ [63]. An example of this type of discharge is shown in figure 15. In this case, $\beta_N \sim 4$, and $H_{89} \sim 2.5$ is sustained for $\sim$2 s in the presence of negative central shear and an internal transport barrier in the ion thermal channel. Stability analysis of these discharges indicate that the achieved β_N is $\sim$30% above the theoretical $\beta_N^{\text{no-wall}}$ while $\beta_N^{\text{ideal-wall}}$ is $\approx$5, indicating a possible path to very high β, fully noninductive operation. Operation at this level of β required simultaneous rotational and feedback stabilization of the resistive wall mode (discussed in section 2.2.2).

The distinguishing feature of this class of fully noninductive discharges is the presence of an internal transport barrier in the ion thermal channel. The measured ion temperature profile near the beginning ($t = 2$ s) and end ($t = 3$ s) of the high performance phase are shown in figure 16(*a*). Transport analysis using TRANSP shown in figure 16(*b*) confirms a reduction in ion transport in this barrier region while electron transport remains relatively high. Note that in this case, the inferred ion thermal diffusivity is below the theoretical 'irreducible minimum' neoclassical prediction.

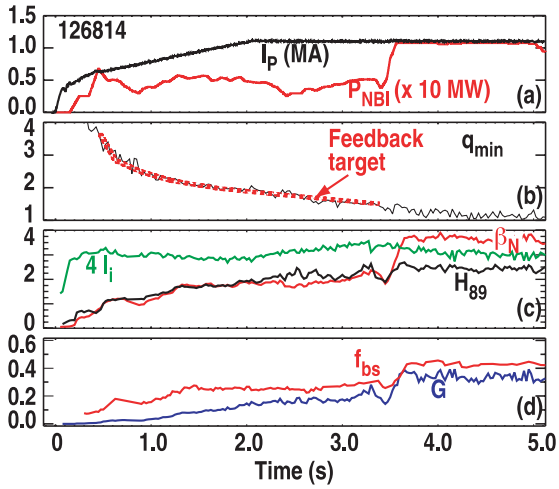

Figure 17. $\beta_N \sim 3.8$, $H_{89} = 2.5$, $G = 0.34$ discharge in which current profile control was used to form the target q profile for the high β phase. Shown are (a) plasma current I_p (black), neutral beam power (red), (b) target (dashed) and real-time measured (red) q_{min} (c) normalized beta β_N (red), confinement quality H_{89} (black) and an estimate of the no-wall beta limit ~4 l_i (green), (d) $G = \beta_N H_{89}/q_{95}^2$ (blue) and bootstrap current fraction f_{bs} (red).

This has been observed in studies previously [64,65]. Attempts to incorporate new aspects of theoretical considerations in hopes of reconciling the observations with the theoretical predictions are still ongoing.

At $t = 2$ s, $G = 0.4$, $\beta_T \sim 4.5\%$ and $f_{bs} = 80\%$. Due to the I_p and B_T ramps at roughly constant β_N, these values continuously change during the high beta phase reaching $G = 0.8$, $\beta_T \sim 7\%$ and $f_{bs} = 60\%$ at 3 s. Detailed analysis of the current profile evolution indicates that the ramps in I_p and B_T act to drive significant off-axis inductive current. Although this means of sustaining the current profile is not compatible with steady-state operation, the excellent stability and transport properties observed in this case confirm theoretical predictions of the benefits of providing off-axis current drive to produce a broad current profile with elevated q_{min}. In fact, stability analysis of a similar discharge suggests that the off-axis current drive provided by the B_T ramp increases β_N^{wall} by nearly a factor of 2 compared with a simulated case without this current drive.

In the second class of discharges [60, 61], an L–H transition is induced early in the current ramp (~400 ms), which broadens the temperature profile and slows down the penetration of the current density. An example of this class of discharge is shown in figure 17. In this discharge, feedback control of the current profile (discussed in section 2.5.2) is utilized to control the evolution of q_{min} such that $q_{min} \sim 2$ at the beginning of the high β phase along with rotational and feedback stabilization of RWMs (discussed in section 2.2.2) during the high β phase. In this case, $\beta_N = 3.8$, $H_{89} = 2.5$, $G = 0.4$, $f_{bs} = 50\%$ is sustained for over 1 s. In a typical discharge of this type, off-axis ECCD supplements the bootstrap current during the high β phase to maintain a broad current profile. However, due to limitations in the available ECCD power, fully noninductive operation was not possible in 2006. Nevertheless, detailed current-drive analysis indicates that the remaining inductive current drive early in the high β phase is localized off-axis. Future experiments using high-power (>2.5 MW) ECCD will seek to replace this off-axis current drive, resulting in fully noninductive operation. The density control capability discussed in section 2.5.3 will be critical in obtaining the necessary current-drive efficiency.

Systematic studies have shown that the β limit is 10%–15% higher in DN plasma shapes compared with previously obtained results in an upper, single-null plasma shape with the same κ and δ. In addition, a strong dependence of the β limit and overall confinement on the details of the plasma shape has been observed in studies in which the outer squareness is varied while maintaining the same κ and δ [66]. The measured dependence of the stability limit on 'squareness' is qualitatively similar to that predicted by previous theoretical stability studies [67]. The observed sensitivity (variations of 10% in β limit and overall confinement) suggests the importance of shape details on performance in ITER [68] and the possibility of a hidden variable that is not accounted for in the standard confinement scalings.

3.2. Hybrid regime

Previous studies on DIII-D (performed with co-NBI only) have documented the development of stationary discharges that offer potential performance enhancements in ITER beyond its $Q = 10$ baseline mission [55, 69]. Recent experiments have extended these results to include high performance operation at low plasma rotation (utilizing the rotation control capabilities outlined in section 2.5.1) and with an ITER-similar shape. An example of a low-rotation, stationary discharge with $q_{95} = 3$ with $G = 0.47$ sustained for over 5 s (or ~5 τ_R) is shown in figure 18. Here, $\tau_R \equiv 0.171 R/\Re$ is the resistive time for current profile relaxation, where R is the major radius and $\Re$ is the plasma resistance in $\mu\Omega$ [70]. The toroidal rotation in this case is roughly a factor of 3 lower than the rotation in previous hybrid discharges at this q_{95}. The achieved performance is somewhat lower than $G = 0.6$ achieved in co-NBI, $q_{95} = 3$ hybrid discharges on DIII-D, but is still well above the normalized performance level required for $Q = 10$ operation in ITER ($G = 0.42$). A similar performance reduction is observed in $q_{95} \sim 4.5$ discharges, but the performance ($G = 0.32$) remains sufficient for $Q \geqslant 5$ in ITER even at this elevated q_{95} level. Other than the decrease in confinement, the beneficial characteristics of hybrid plasmas (sawteeth mitigation, benign NTMs, high beta operation) are retained in these low-rotation cases.

In addition to low-rotation operation, the space over which these improved performance conditions can be sustained has been significantly expanded over the past few years and now includes $0.9 < B_T(T) < 2.1$, $0.7 < I_p(\mathrm{MA}) < 1.7$, $2.8 < q_{95} < 5.0$, $0.5 < \langle\delta\rangle < 0.65$, $0.35 < n_e/n_{GW} < 0.75$, $0.004 < M_\phi < 0.5$, $1.1 < T_i/T_e < 1.5$ and $f_{rad} < 60\%$. This expansion of the operating space has enabled a variety of studies aimed at understanding transport in this regime as well as assessing the compatibility of this regime with anticipated ITER-like conditions, such as low rotation and high radiative power fractions. Detailed transport analysis of individual discharges indicates that both the ion and the electron thermal diffusivity are generally small in this class of discharges with $\chi_e > \chi_i$ (figure 6).

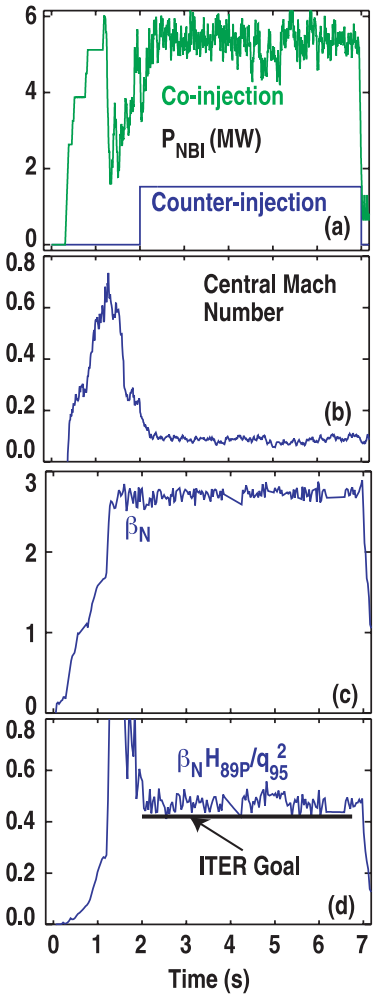

Figure 18. Temporal evolution of a low-rotation, hybrid discharge at $q_{95} = 3.2$ with performance in excess of the requirements for $Q = 10$ in ITER. Shown are (*a*) co- (green) and counter- (blue) NBI power, (*b*) central Mach number, (*c*) normalized beta β_N and (*d*) $G = \beta_N H_{89}/q_{95}^2$. The performance objective of the ITER $Q = 10$ baseline scenario is denoted in (*d*).

These observations are consistent with nonlinear GYRO [71] simulations that show electron temperature-gradient (ETG) modes and trapped electron modes (TEMs) cause the majority of transport even though these modes are predicted to be linearly stable in the core. In addition, gyroradius ρ^* scaling studies have shown that local thermal diffusivity scales in near gyroBohm-like fashion in the core but more Bohm-like near the edge, similar to standard H-mode plasmas at the same q_{95} [72]. In addition, ECE measurements indicate the presence of a $m = 2/n = 2$ sideband to the $m = 3/n = 2$ NTM as q_0 approaches unity, which is an essential ingredient in a recently developed theory aimed at explaining the effect of the $m = 3/n = 2$ on maintaining $q_0 > 0$ in these discharges [73].

The compatibility of enhanced performance plasmas with high radiative power fractions has been demonstrated using argon injection into otherwise stationary hybrid, USN plasmas with $\beta_N = 2.6$ s $H_{89} = 2.1$, and $G = 0.4$ [74]. In these discharges, the standard 'puff-and-pump' technique [75] is used in which the argon is introduced into the upper divertor region and strong deuterium fuelling is introduced into the scrape-off layer (SOL) in the lower divertor region. Using this technique, high values of argon enrichment in the divertor region ($\eta_{Ar} \sim 30$) are inferred from measurements of the argon concentrations in the core and pumping plenum regions. This high argon enrichment permits high radiative fractions (63%) and a factor of 2 decrease in divertor heat flux with minimal core dilution (f_{Ar}, core $= 0.2\%$) and negligible impact on β_N, H_{89} or G.

4. Advances in scientific understanding

Enabled by significant advances in diagnostic capabilities and the aforementioned control tool set, the DIII-D programme has advanced significantly the understanding of key processes that govern plasma performance. These advances are aimed at providing the ability to predict all aspects of fusion plasma performance, thereby providing a means to improve the efficiency and effectiveness of experiments in ITER and gaining the greatest scientific benefit from ITER operation. Examples of some of the key recent advances in areas important for ITER success are discussed in this section.

4.1. Energetic particles

Energetic-particle-driven instabilities could pose a significant threat to plasma facing surfaces and to the achievement of adequate plasma performance in ITER. Hence, developing predictive models of these instabilities before ITER operates is essential for its operation and optimization. Enabled by significant advances in diagnostic capabilities on DIII-D, direct measurements of the spatial structure of toroidal Alfvén eigenmodes (TAEs) and reversed shear Alfvén eigenmodes (RSAEs) are now routinely available, enabling the measurement of instabilities with toroidal mode numbers approaching 40 [76]. An example of the measured radial structure from spatially resolved electron cyclotron emission (ECE) measurements of the electron temperature perturbations is shown in figure 19 [77], along with a comparison of the predicted perturbation by the ideal MHD code NOVA [78]. The ECE perturbations shown here are $\delta T_e = A \cos t(\phi - \phi_{ref})$ where the amplitude A and phase ϕ are determined by Fourier analysis of the ECE data and ϕ_{ref} is the phase from the channel with the largest perturbation. Since NOVA is a linear code and therefore cannot predict the amplitude of the perturbations, the NOVA prediction in figure 19 has been scaled to match the measured perturbation amplitude, thereby providing a normalization for $\delta B/B$ for the NOVA predictions. Using this normalization, good quantitative agreement has been found between the NOVA calculation and the amplitude of the measured density fluctuations from beam emission spectroscopy (BES) and reflectometry, bolstering the validity of the NOVA predictions [77].

Of critical interest for ITER is the impact that these instabilities will have on the alpha particle distribution. Such effects can now be measured on DIII-D using the fast-ion D_α (FIDA) diagnostic [79]. An example is shown in figure 20, which shows a direct correlation between the level of Alfvén

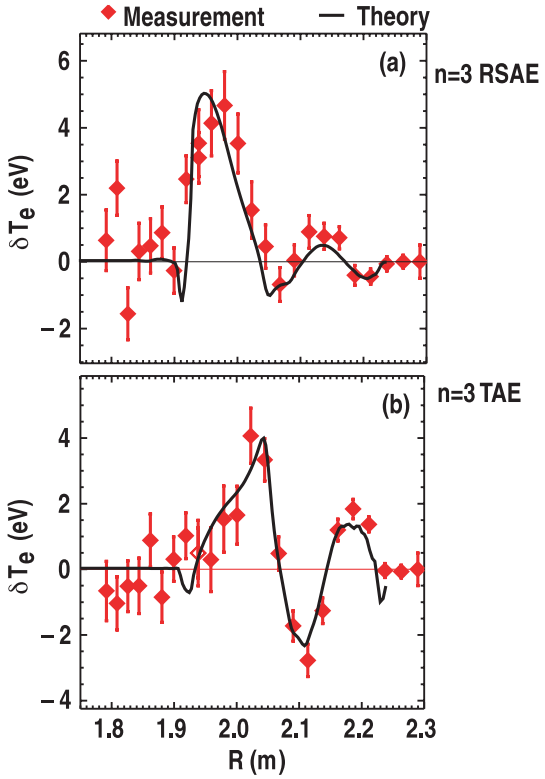

Figure 19. Measured (symbols) and predicted (lines) T_e perturbation due to (*a*) $n = 3$ RSAEs and (*b*) $n = 3$ TAEs on the outboard midplane of DIII-D.

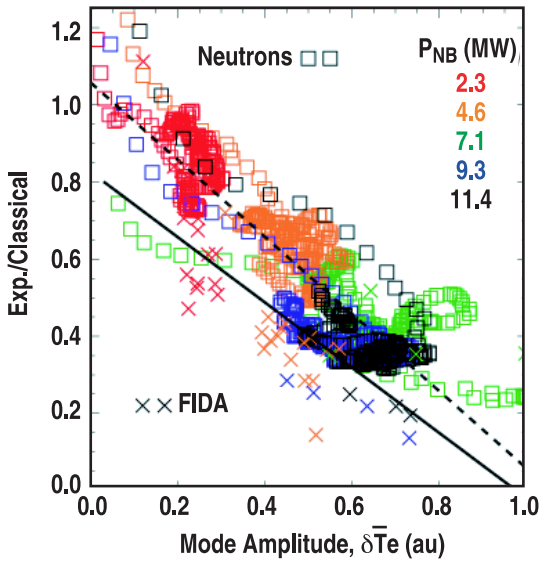

Figure 20. Inferred deficit of the measured neutrons (squares) and fast-ion density as measured by a FIDA channel near q_{min} (X) relative to the value expected from classical slowing down of the fast ions as a function of TAE mode amplitude. The varying colours represent a sequence of discharges with different values of beam power. Mode amplitude ($\delta\bar{T}_e$) is a measure of the average electron temperature perturbation of the 10 largest modes.

eigenmode activity and the deficit in the fast-ion density (relative to the classically predicted value). This deficit is even larger than the deficit in the measured neutron rate relative to the classically expected value.

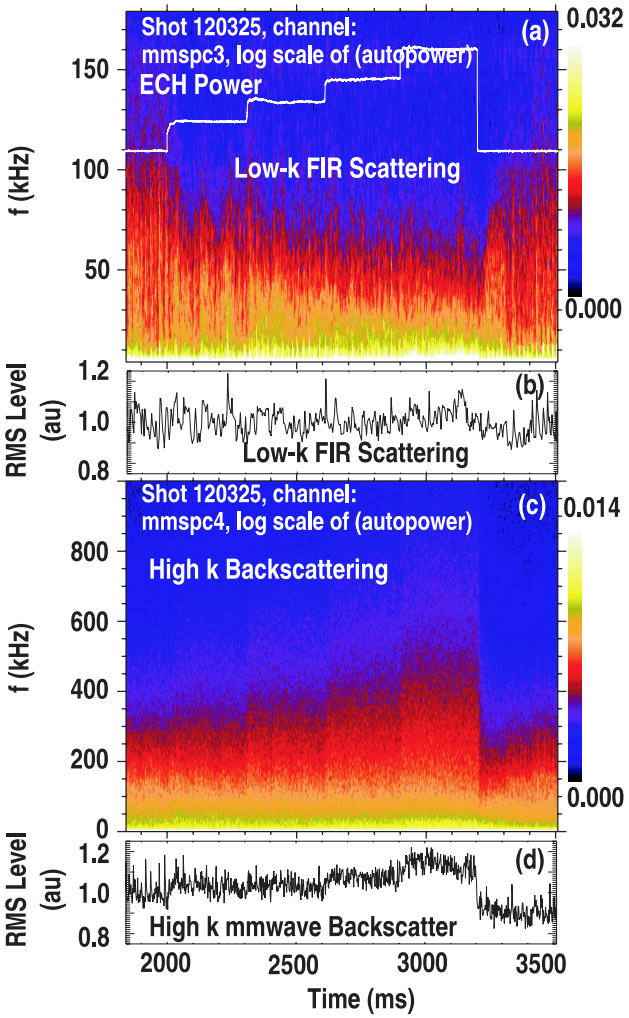

Figure 21. Comparison of the frequency spectra and normalized fluctuation levels $\tilde{n}/n$ for low-k (*a*) and (*b*) and high-k (*c*) and (*d*) fluctuations during an ECH power scan (shown in white traces in (*a*)–(*c*).

4.2. Turbulence and zonal flow characterization

Because of the significantly smaller scale of transport processes relative to macroscopic stability processes, control and optimization of transport is generally more difficult and requires a more thorough understanding of the basic underlying processes. Over the past decade, tokamak experiments worldwide have shown that electrostatic turbulence is generally the dominant process causing radial transport of energy and particles. Over this same time period, sophisticated numerical codes that capture the basic physics of electrostatic turbulence in full toroidal geometry have been developed, providing a platform for studying the underlying processes in detail. To provide data for validating the predictions of these codes, the DIII-D diagnostic set has been enhanced recently to provide turbulence measurements at all relevant scale lengths ($1\,\mathrm{cm}^{-1} < k_\perp < 35$–$40\,\mathrm{cm}^{-1}$), providing new information on the details of the turbulence-driven transport. An example of this capability is shown in figure 21 in which the power spectra from low k ($\sim 1\,\mathrm{cm}^{-1}$) by far infrared (FIR) scattering and high k ($\sim 35\,\mathrm{cm}^{-1}$) measurements using microwave backscattering are shown [80]. Both measurements

are line-integrated measurements with the FIR scattering data originating along a chord oriented radially along the plasma midplane while the high k measurements sample a chord lying near the midplane which begins at the outboard edge and ends on the low field side at $\rho \approx= 0.4$. In this case, the response of the turbulence at different spatial scales to changes in the ECH power is observed to be quite different with the high k turbulence levels increasing while the low k fluctuation levels remain approximately constant. These results indicate that the high k turbulence is decoupled from the lower k turbulence, suggesting that the turbulent drive at small-scale lengths is not primarily due to turbulence at longer wavelengths. This unique capability has allowed detailed characterization of turbulence at multiple scale lengths, identification of turbulence-driven zonal flows and the role of these zonal flows in regulating turbulence levels. Examples of several key discoveries and insights from the DIII-D are presented in this section.

A recent modification of the DIII-D microwave backscattering system [81] has enabled localized measurements of small-scale turbulence ($k_\perp = 35\,\mathrm{cm}^{-1}$), which is theoretically predicted to be driven unstable by ETG modes. Measurements at various radial locations during ECH and NBI heating indicate that the turbulence response at each location is different and that this response is dependent on the method used for plasma heating. In the edge, the turbulence levels are observed to increase markedly during the ECH while the core turbulence is either unaffected or reduced. In contrast, during short NBI blips, the core turbulence is observed to increase markedly while the edge turbulence is only slightly affected. Preliminary analysis using the linear gyrokinetic stability code GKS [82] indicates that the linear growth rates in the edge region increase markedly during the ECH phase while the core growth rates decrease [83]. Nonlinear simulations utilizing diagnostic filters to simulate experimental diagnostics are underway.

A key insight garnered from theory and confirmed by experiment over the past few years has been the important role that zonal flows play in regulating turbulence-driven transport. Zonal flows are radially localized, poloidally and toroidally uniform ($n = 0$, $m \cong 0$) electrostatic fluctuations that are excited by drift wave turbulence, removing free energy from the underlying turbulence and thereby regulating the transport process [84]. Detailed analysis of data from the upgraded DIII-D BES system [85] has identified and characterized two classes of zonal flows—the geodesic acoustic mode (GAM) and the zero-mean-frequency (ZMF) zonal flow (figure 22) [86]. GAMs are moderate frequency (∼15 kHz) zonal flows that exist primarily near the periphery of the plasma ($0.85 < r/a < 0.95$) and that increase strongly as the edge safety factor increases [87]. Time-delay-estimation (TDE) techniques indicate that the GAMs not only modulate the intensity of the underlying turbulence but also act to drive a transfer of internal energy from low to high frequencies, as predicted by theory [88]. The ZMF zonal flow is a low-frequency, spectrally broad ($\Delta f \sim 10$ kHz) poloidal flow structure that peaks near zero frequency in the plasma core region ($0.6 < r/a < 0.9$) [89]. Consistent with theoretical predictions, these ZMF zonal flows are characterized by a poloidal correlation length of the velocity fluctuations that is significantly longer than

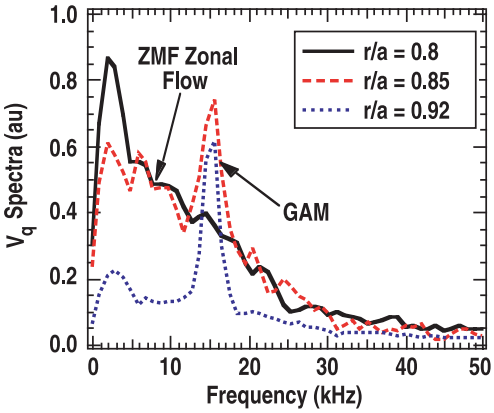

Figure 22. Poloidal velocity fluctuation spectra at three radial locations measured by beam emission spectroscopy (BES), exhibiting a transition from a GAM dominated spectrum near the edge to the ZMF zonal flow dominated spectrum towards the core.

the poloidal correlation length for density fluctuations and a radial correlation length of the poloidal velocity fluctuations (∼1–2 cm) comparable to the background turbulence radial correlation length.

In addition to regulating turbulence-driven transport, DIII-D measurements [90] coupled with GYRO simulations suggest that zonal flows play an important role in the formation of internal transport barriers near low order rational q values that has been commonly observed in negative central shear (i.e. $q_{\min}$ located off-axis) plasmas worldwide [91–94]. In these discharges, high time-resolution ECE and CER measurements indicate simultaneous improvements in electron and ion thermal transport just before $q_{\min}$ reaches a low-order rational value. In addition, BES measurements indicate that long-wavelength turbulent fluctuations decrease concurrent with an increase in the poloidal flow velocity and flow shear just before $q_{\min}$ reaches a rational value. These observations are qualitatively consistent with GYRO simulations that predict 'profile corrugations' associated with time-averaged components of zonal flows near the rational surface [95]. These localized zonal flows can be very large due to the local minimum in the density of low-order rational surfaces, leading to suppression of the turbulence near the rational surface and increases in the temperature gradients. Note that the oscillating $E \times B$ shear associated with these zonal flows is superimposed on top of the equilibrium $E \times B$ shear. When the magnitude of the equilibrium $E \times B$ shear alone is marginal for decorrelating the underlying turbulence, the increased $E \times B$ shear caused by zonal-flow-induced changes in transport can be the trigger for the formation of a sustained core transport barrier. Experiments have shown that in cases in which the background $E \times B$ shear is insufficient, transient reductions in transport are observed but do not lead to the formation of a core transport barrier.

4.3. Edge/material surface optimization and understanding

DIII-D is well positioned to provide the physics basis for carbon-based plasma facing materials owing to its ∼95% coverage of the main chamber walls with graphite tiles. General experience with carbon facing components worldwide

has shown the compatibility of these components with a wide range of operating regimes, including high performance regimes. The primary drawback for carbon's use in ITER is tritium retention in re-deposited layers of carbon. A key mission of the near-term DIII-D research is to provide the physics basis for the choice of carbon as a primary plasma facing material in ITER. To this end, recent experiments on DIII-D have documented the migration path of artificially introduced carbon in ELMing H-mode plasmas, demonstrated that deuterium co-deposition with carbon is dramatically reduced in heated materials and established the capability to produce and sustain high performance plasmas on de-conditioned graphite walls.

4.3.1. Carbon transport and deposition. Experiments using carbon-13 as a tracer impurity have been utilized to study the migration path of carbon in detached ELMing H-mode plasmas. $C^{13}H_4$ was injected into the upper divertor plenum of DIII-D over a reproducible series of lower-single-null discharges at the very end of an experiment campaign. Analysis of a set of graphite tiles removed immediately following $C^{13}H_4$ injection into a reproducible set of detached, ELMing H-mode discharges shows that the largest deposition of C^{13} was localized to the inner divertor and private flux region [96]. The inner divertor deposition profile is qualitatively very similar to that measured in previous $C^{13}H_4$ injection experiments in L-mode plasmas [97] while the private flux region deposition appears to be specific to the ELMing H-mode case. Based on measurements showing toroidal symmetry of the deposition, approximately 40% of the injected C^{13} is deposited in the lower divertor region. High sensitivity analysis indicates that small levels of C^{13} are deposited on the inner wall and regions near the aperture from the upper plenum to the main chamber. The measured deposition patterns in the divertor region in both the L-mode and the H-mode cases have been qualitatively reproduced in two-dimensional edge modelling using an ad hoc parallel flow with a Mach number $M \sim 0.4$ directed towards the inner divertor in conjunction with an imposed inward convection ($V_{\text{pinch}} \sim 10\,\text{m}\,\text{s}^{-1}$) above the divertor region [98–100]. Note that in the H-mode case, no attempt has been made to model the values of M and V_{pinch} in the ELM-free and ELMing phases separately and, therefore, represent an average over these phases.

Separate studies using the DIII-D DiMES system have shown that the amount of deuterium co-deposition in carbon deposits is quite sensitive to the temperature of the exposed samples. In particular, experiments exposing a simulated tile gap in the outer divertor region showed that the deuterium co-deposition was reduced by a factor of 10 when the tile gap was heated to 150 °C as opposed to room temperature (figure 23) [101]. Similar experiments that exposed molybdenum mirrors to divertor conditions also showed a dramatic reduction in carbon deposition on the mirror surfaces [102]. These results, combined with results from C^{13} transport studies suggest a possible solution to the tritium retention issue in ITER by heating of the inner divertor substrate.

Using Raleigh/Mie scattering from the ND : YAG lasers used for Thomson scattering measurements, quantitative measurements of dust characteristics in the DIII-D scrape-off layer (SOL) are now possible [103]. Time-averaged dust

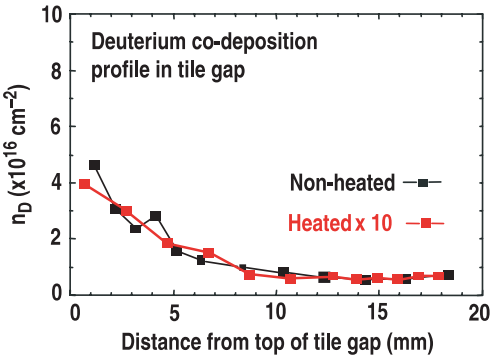

Figure 23. Measured profile of deuterium co-deposition from *ex situ* analysis of a simulated tile gap exposed to a series of reproducible plasmas using the DIII-D DiMES system when exposed at room temperature (black) and at 150 °C (red). Note that the scale of the heated sample has been scaled by a factor of 10.

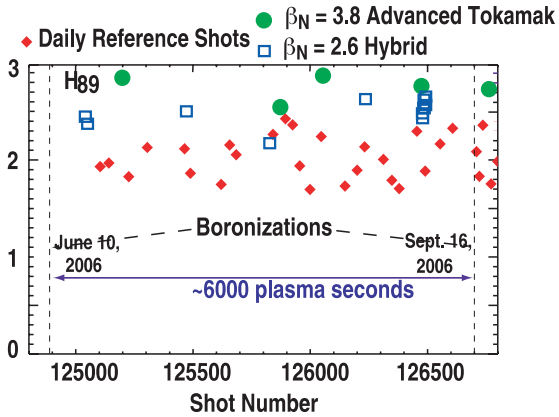

Figure 24. Confinement quality versus shot number during the 2006 experimental campaign of conventional, H-mode reference shots (red diamonds), hybrid discharges (blue squares), and advanced tokamak plasmas (green circles). The two boronizations during the 2006 campaign are denoted as the vertical dashed lines.

concentrations as high as 6000 m^{-3} are observed in the far SOL and drop to near zero at the last closed flux surface. The average radius of these dust particles is ~80 nm [104]. Statistical studies indicate a dust mean number density of 4000 m^{-3}, corresponding to a carbon atom density of 10^{13}m^{-3}, which is 5 orders of magnitude lower than the core carbon density. This strongly suggests that these dust particles are not a major source of core carbon contamination. The measured dust density has been found to be sensitive to the plasma conditions with the maximum dust generated in conditions with ELMs, high pedestal temperatures and small gaps between the plasma and walls.

4.3.2. Effect of wall conditioning on performance. Finally, a recent set of experiments in DIII-D has demonstrated the ability to access and sustain high performance plasmas without routine boronization. The result of this assessment is shown in figure 24 in which the confinement obtained during the stationary phase of various types of discharges from the 2006 experimental campaign is shown. During this experimental campaign, only two boronizations were conducted—one near the beginning following a week of plasma operation and

one near the end followed by roughly a week of plasma operation. Throughout this period, a series of reference shots were taken to evaluate wall conditioning and its effect on plasma performance. Three types of reference shots were taken: daily reference shots (diamonds in figure 24), which contain a low-power, H-mode phase, stationary, hybrid discharges (squares) with $\beta_N = 2.6$ and advanced tokamak discharges (circles) with $\beta_N = 3.8$. For all discharge types, confinement remains nearly constant over the entire inter-boronization period. Of note is the fact that the hybrid and advanced tokamak discharges obtained after ~6000 s of plasma operation without boronization exhibit comparable performance in terms of β_N, H_{89} and G as those taken early in the period. In fact, in the advanced tokamak case, the normalized performance is among the highest ever achieved on DIII-D.

Near the end of the inter-boronization period, a dedicated experiment was carried out to assess the impact of between-shot wall conditioning (most notably helium glow cleaning) on the performance capabilities. Seven identically prepared, long-pulse ($\tau_{dur} > 2\tau_R$), moderate performance ($\beta_N \sim 2.6$, $H_{89} \sim 2.4$, $G = 0.38$) hybrid discharges with strong divertor pumping (the cluster of blue squares in figure 24) showed no evidence of performance deterioration without any between-shot wall conditioning. Even with gas injection levels of ~20 Torr ℓ s^{-1} to maintain an line-averaged density of 5×10^{19} m^{-3}, particle balance measurements indicate that the divertor cryopumps are providing more particle exhaust than is being injected via neutral beams and gas injection. These results suggest that graphite wall conditions adequate to obtain high performance plasmas can be maintained over an extended period without conditioning provided sufficient particle exhaust is available to maintain good particle balance on a shot-to-shot basis. This is in marked contrast to recent results from Alcator C-Mod [105] in which routine conditioning of high-Z walls is required to access high performance regimes. Two reasons have been speculated for the reduced dependence on boronization in DIII-D. First, with the installation of upper divertor baffles and cryopumps in 1997 followed more recently with the modifications of the lower divertor in 2005, the majority of DIII-D discharges have strong active particle exhaust. It has been demonstrated experimentally [106] that strong divertor exhaust maintains a low uptake of deuterium by the plasma facing wall, reducing the need for off-line wall conditioning. In this respect, DIII-D is unique in the world in its ability to maintain good density control in high confinement regimes. This is probably the primary reason behind the ability to reduce the rate of boronization events. The second possibility is that the use of regular boronization on DIII-D [107] since all the graphite tiles were replaced in 1993 (total of 64 boronization depositions) has led to the development of a boron reservoir within the vessel. While some tiles have been replaced over the years, most of the outer wall tiles have remained in place and provide a large surface area (~20 m^2) of boron mixed with other eroded materials from other locations. Because the surfaces in which this boron reservoir is located (outer wall) is not the same as the surfaces where the primary plasma contact occurs (divertor region), this reservoir is expected to have a small impact on plasma performance.

5. Summary and outlook

As demonstrated by the results presented above, the DIII-D research programme has made significant progress in the development of physics solutions to key issues facing ITER, in demonstrating the promise of advanced operating regimes for ITER and in providing key insights into basic fusion plasma processes. Through this research and development, the DIII-D research programme has provided additional confidence that ITER can achieve its basic research mission tasks and established the physics basis for a potentially enhanced experimental programme on ITER extending well beyond its baseline mission (i.e. the potential of $Q > 10$ operation).

Future research on DIII-D will focus on three basic themes: (1) enabling the success of ITER by providing physics solutions to key ITER issues, (2) developing the physics basis of steady-state, high performance tokamak operation and (3) advancing the fundamental understanding of fusion plasmas. In the near term, the highest emphasis will be placed on providing the physics basis for urgent ITER design issues. Key design issues to be addressed include the use of internal coils for ELM suppression and RWM stabilization, startup requirements for access to advanced regimes, the choice of plasma facing materials, NTM stabilization via ECCD and disruption mitigation. Following the finalization of the ITER baseline design, the research focus will shift to the development and qualification of advanced operating regimes for use in ITER. This research will seek to demonstrate the performance capabilities of these advanced regimes in ITER-like conditions (e.g. low rotation, $T_e \approx T_i$, highly radiative conditions), develop the physics basis for the extrapolation of these regimes to ITER and determine the control requirements necessary for realization of these regimes in ITER.

The DIII-D Advanced Tokamak research programme will focus in the near term on utilizing increased EC and fast-wave power to demonstrate fully noninductive, steady-state operation for longer than a current relaxation time (~2 s), which would provide a strong basis for $Q = 5$, steady-state operation in ITER. Simultaneously, exploratory research will be undertaken to determine the ultimate limits of high β, steady-state operation, focusing on transient demonstrations of high performance in the near term. Based on the results of this exploration, a dedicated effort will be made in the intermediate term to demonstrate such performance in steady-state conditions.

In addition to the directed research for ITER support and Advanced Tokamak development, DIII-D will also continue to advance the fundamental understanding of key processes in fusion plasmas utilizing the recent upgrades of the neutral beam, electron cyclotron, divertor and diagnostic systems. Emphasis will be placed on developing an improved understanding of turbulence-driven transport, energetic-particle-driven instabilities and their impact and scrape-off-layer flows. This research will help to ensure that the greatest scientific benefit can be obtained from ITER operation and provide the basis for predictive control in the optimization of the tokamak approach to fusion energy production.

Acknowledgment

This work was supported by the US Department of Energy under DE-FC02-04ER54698.

Appendix. The DIII-D Team

G. Abla,[1] S.L. Allen,[2] P.M. Anderson,[1] R. Andre,[3] G. Antar,[4] M.E. Austin,[5] F.W. Baity,[6] J.P. Bakalarski,[1] D.R. Baker,[1] M. Bakhtiari,[7] D.E. Baldwin,[1] D.E.G. Barber,[6] V. Basiuk,[8] R. Bastasz,[9] C.B. Baxi,[1] L.R. Baylor,[6] M. Becoulet,[8] E.A. Belli,[1] H.L. Berk,[5] J.M. Bialek,[10] J. Blair,[11] J.A. Boedo,[4] I.N. Bogatu,[12] R.L. Boivin,[1] R.V. Bravenec,[5] B.D. Bray,[1] D.P. Brennan,[13] S. Brezinsek,[14] N.H. Brooks,[1] R.V. Budny,[3] K.H. Burrell,[1] R.J. Buttery,[15] O. Buzhinskij,[16] J.D. Callen,[7] R.W. Callis,[1] G.L. Campbell,[1] J.M. Candy,[1] T.N. Carlstrom,[1] W.P. Cary,[1] T.A. Casper,[2] V.S. Chan,[1] M.S. Chance,[3] E. Chin,[1] H.K. Chiu,[1] M. Choi,[1] M.S. Chu,[1] S. Cirant,[17] R.J. Colchin,[6] S.K. Combs,[6] J. Culver,[18] J.W. Davis,[18] W. Davis,[3] J.S. deGrassie,[1] J.C. DeBoo,[1] J.L. Doane,[1] R.P. Doerner,[4] V. Dokouka,[16] J. Dorris,[13] E.J. Doyle,[19] F. Dubois,[8] D.H. Edgell,[20] D. Elder,[18] R.A. Ellis, III,[3] R.F. Ellis,[21] C. Estrada-Mila,[4] T.E. Evans,[1] E. Feibush,[3] M.E. Fenstermacher,[2] J.R. Ferron,[1] K.H. Finken,[14] D.K. Finkenthal,[22] R.K. Fisher,[1] S.M. Flanagan,[1] R.J. Fonck, [7] C-M. Fransson,[23] E. Fredd,[3] E.D. Fredrickson,[3] G.Y. Fu,[3] S.A. Galkin,[24] Q. Gao,[25] A.M. Garofalo,[10] K.W. Gentle,[5] R. Gianella,[8] M. Gilmore,[26] P. Gohil,[1] X. Gong,[25] I.A. Gorelov,[1] N.N. Gorelenkov,[3] R.H. Goulding,[6] R. Granetz,[13] M.T. Green,[1] K.L. Greene,[1] C.M. Greenfield,[1] N.L. Greenough,[3] R.J. Groebner,[1] M. Groth,[2] H.J. Grunloh,[1] M. Graznevitch,[15] S. Günter,[27] D. Gupta,[7] T.S. Hahm,[3] K. Halletschek,[27] M.J. Hansink,[1] R.J. Harrington,[28] J.H. Harris,[29] S. Harrison,[7] R.W. Harvey,[30] R. Hatcher,[3] N.C. Hawkes,[15] C.C. Hegna,[7] W.W. Heidbrink,[31] T.C. Hender,[15] D.N. Hill,[2] F.L. Hinton,[1] J.T. Hogan,[6] C. Holcomb,[2] C. Holland,[4] E.M. Hollman,[4] K.L. Holtrop,[1] R.-M. Hong,[1] J.C. Hosea,[3] N. Howard,[32] D.F. Howell,[15] W.A. Houlberg,[6] C.-L. Hsieh,[1] C. Hu,[25] D.A. Humphreys,[1] P. Huynh,[1] A.W. Hyatt,[1] F. Imbeaux,[8] Y. In,[12] K. Indireshkumar,[3] A. Isayama,[33] R.C. Isler,[6] G.L. Jackson,[1] A.M. Jacques,[1] M. Jakabowski,[14] A.N. James,[4] S.C. Jardin,[3] R.J. Jayakumar,[2] T.C. Jernigan,[6] H. Jhang,[34] E.H. Joffrin,[8] R.D. Johnson,[1] I. Joseph,[4] K. Kajiwara,[35] D.H. Kaplan,[1] S. Kasiloz,[36] O. Katsuro-Hopkins,[10] J.-Y. Kim,[25] K.M. Keith,[1] A.G. Kellman,[1] D.H. Kellman,[1] M.A.H. Kempenaars,[37] C. Kessel,[3] R. Khayrutdinov,[16] C. Kim,[7] J.S. Kim,[12] L. Kim,[1] J.E. Kinsey,[11] W.-H. Ko,[34] G.J. Kramer,[3] S.I. Krasheninnikov,[4] K. Krieger,[27] S.E. Kruger,[38] R.J. La Haye,[1] L.L. Lao,[1] C.J. Lasnier,[2] E.A. Lazarus,[6] J.-N. Leboeuf,[19] H. Lee,[34] R.L. Lee,[1] X. Lee,[1] M. Lehnen,[14] A.W. Leonard,[1] J.A. Leuer,[1] Y.R. Lin-Liu,[39] S. Lisgo,[18] A. Litnovsky,[14] C. Liu,[1] Y.Q. Liu,[40] A. Loarte,[27] J. Lohr,[1] J. Lonnroth,[41] T.C. Luce,[1] C. Ludescher-Furth,[3] Y. Luo,[31] J.L. Luxon,[1] M.A. Mahdavi,[1] J. Mailloux,[15] R. Maingi,[6] C.C. Makariou,[1] M.A. Makowski,[2] J. Manickam,[3] A. Manini,[27] M.E. Maraschek,[27] G. Matsunaga,[33] P.S. Mauzey,[1] D. Mazon,[8] D.C. McCune,[3] B.B. McHarg,[1] G.R. McKee,[7] A.G. McLean,[18] J.E. Menard,[3] W.H. Meyer,[2] D. Mikkelsen,[3] C.P. Moeller,[1] J.M. Moller,[2] P. Monier-Garbet,[8] R.A. Moyer,[4] A. Mui,[22] M. Murakami,[6] C.J. Murphy,[1] A. Nagy,[3] E. Nardon,[8] M.F.A. Nave,[42] G.A. Navratil,[10] R. Nazikian,[3] A. Nerem,[1] X.V. Nguyen,[19] H. Nishino,[43] S. Noraky,[1] T. Oikawa,[33] M. Okabayashi,[3] R.A. Olstad,[1] T.H. Osborne,[1] L.W. Owens,[6] Y. Ou,[11] N.A. Pablant,[4] V. Parail,[44] J.-M. Park,[34] Y.-S. Park,[45] C.T. Parker,[1] P.B. Parks,[1] C.J. Pawley,[1] J.J. Peavy,[1] W.A. Peebles,[19] B.G. Penaflor,[1] Q. Peng,[1] F.W. Perkins,[3] P.I. Petersen,[1] T.W. Petrie,[1] C.C. Petty,[1] N.Q. Pham,[1] J.C. Phillips,[1] V. Phillips,[14] S.D. Pinches,[27] A.Yu. Pigarov,[4] D.A. Piglowski,[1] R.I. Pinsker,[1] P.A. Politzer,[1] D. Ponce,[1] D.M. Ponce,[35] M. Porkolab,[13] G.D. Porter,[2] R. Prater,[1] D.G. Pretty,[29] L.E. Randerson,[3] D.A. Rasmussen,[6] H. Reimerdes,[10] E.E. Reis, Jr.,[1] M.E. Rensink,[2] G. Rewoldt,[3] T.L. Rhodes,[19] T.D. Rognlien,[2] L. Roquemore,[3] D.W. Ross,[5] J.C. Rost,[13] D.L. Rudakov,[4] A. Runov,[46] E. Ruskov,[31] F. Ryter,[27] Y. Sakamoto,[33] G. Saibene,[27] O. Sauter,[47] R.I. Savercool,[1] M.J. Schaffer,[1] D.P. Schissel,[1] D.J. Schlossberg,[7] L. Schmitz,[19] O. Schmitz,[14] D.D. Schnack,[48] M. Schneider,[8] R. Schneider,[46] E. Schuster,[11] J.T. Scoville,[1] D. Sellers,[1] M.W. Shafer,[7] A. Shaw,[1] B. Shen,[25] K.C. Shoolbred,[1] A.C.C. Sips,[27] A.P. Smirnov,[49] P.B. Snyder,[1] E.R. Solano,[50] W.M. Solomon,[3] W.M. Stacey,[51] G.M. Staebler,[1] R.D. Stambaugh,[1] P.C. Stangeby,[18] R. Stemprok,[1] H.E. St John,[1] E.J. Strait,[1] D. Szymanski,[1] H. Takahashi,[3] M. Takechi,[33] D. Taussig,[1] P.L. Taylor,[1] T.S. Taylor,[1] R.J. Temkin,[13] T.B. Terpstra,[1] D.M. Thomas,[1] P.R. Thomas,[8] J.F. Tooker,[1] A.D. Turnbull,[1] G.R. Tynan,[4] M.A. Ulrickson,[9] B. Unterberg,[14] H. Urano,[33] E. Valeo,[3] M.A. VanZeeland,[1] S. Visser,[1] F. Volpe,[52] M.R. Wade,[1] F.L. Waelbroeck,[5] R. Wagner,[4] M.L. Walker,[1] R.E. Waltz,[1] W.R. Wampler,[9] B. Wan,[53] A. Wang,[25] G. Wang,[19] H. Wang,[25] J.G. Watkins,[9] G.W. Watson,[31] A.S. Welander,[1] J.C. Wesley,[1] W.P. West,[1] J. Whaley,[9] A.E. White,[19] R. White,[3] D.G. Whyte,[13] H.R. Wilson,[15] C.P.C. Wong,[1] K.L. Wong,[3] S.K. Wong,[1] L. Yan,[25] L. Yang,[25] H.H. Yip,[1] J. Yu,[4] L. Zeng,[19] C. Zhang,[53] D. Zhou,[53] Y. Zhu[31]

[1] General Atomics, USA
[2] Lawrence Livermore National Laboratory, USA
[3] Princeton Plasma Physics Laboratory, USA
[4] University of California, San Diego, USA
[5] University of Texas at Austin, USA
[6] Oak Ridge National Laboratory, USA
[7] University of Wisconsin, Madison, USA
[8] CEA Cadarache Euratom Association, France
[9] Sandia National Laboratories, USA
[10] Columbia University, USA
[11] Lehigh University, USA
[12] FARTECH, Inc., USA
[13] Massachusetts Institute of Technology, USA
[14] FZ-Julich Euratom Association, Germany
[15] UKAEA Fusion Culham Science Centre, UK
[16] Troitsk Institute of Innovative & Thermonuclear Investigations, Russia
[17] ENEA, Frascati, Italy
[18] University of Toronto, Canada
[19] University of California, Los Angeles, USA
[20] LLE, University of Rochester, USA
[21] University of Maryland, USA
[22] Palomar Community College, USA
[23] Tomlab Optimization Inc., USA

[24] Keldysh Institute, Russia
[25] SWIPP, Chengdu, China
[26] University of New Mexico, USA
[27] Max-Planck-Institut für Plasmaphysik, Germany
[28] Rensselaer Polytechnic Institute, USA
[29] Australian National University, Australia
[30] CompX, USA
[31] University of California, Irvine, USA
[32] University of Illinois, USA
[33] Japan Atomic Energy Agency (JAEA), Japan
[34] National Fusion Research Center, Korea
[35] Oak Ridge Institute of Science Education, USA
[36] Kharkov Institute for Physics & Technology
[37] FOM-Rijnhuizen, The Netherlands
[38] Tech-X, USA
[39] Dong Hua University, China
[40] Chalmers University, Sweden
[41] Helsinki University, Finland
[42] EURATOM/IST, Lisbon
[43] Hiroshima University, Japan
[44] Culham, UKAEA, UK
[45] Seoul University, Korea
[46] Max Planck Institute, Griefswald, Germany
[47] CRPP-EPFL, Lausanne, Switzerland
[48] SAIC, USA
[49] Moscow State University, Russia
[50] EURATOM/CIEMAT, Madrid, Spain
[51] Georgia Institute of Technology, USA
[52] Max-Planck, Gesellschaft, Germany
[53] ASIPP, Hefei, China

References

[1] Aymar R., Barabaschi P. and Shimomura Y. (ITER Team) 2002 *Plasma Phys. Control. Fusion* **44** 519
[2] Luce T.C. for the DIII-D Team 2005 *Nucl. Fusion* **45** S86
[3] Burrell K.H. and the DIII-D Team 2003 *Nucl. Fusion* **43** 1555
[4] Luxon J.L., Simonen T.C., Stambaugh R.D. and the DIII-D Team 2005 *Fusion. Sci. Technol.* **48** 807
[5] Anderson P.M., Baxi, C.B., Kellman A.G., Reis E.E. and Robinson J.I. 2003 *Fusion Eng. Des.* **66–68** 791
[6] Jackson G.L. *et al* 2006 *Proc. 33rd EPS Conf. on Plasma Physics (Rome, Italy, 2006)* vol 30I (ECA) P-5.143
[7] Schaffer M.J., La Haye R.J., Strait E.J., Garofalo A.M., Hyatt A.W., Jacques A.M., Leuer J.A. and Scoville J.T. 2006 *Bull. Am. Phys. Soc.* **51** 268
[8] Robinson J.I. and Scoville J.T. 1996 *Proc. 16th IEEE/NPSS Symp. on Fusion Engineering (Champaign, Illinois)* vol 1 (Piscataway, NJ: IEEE) p 829
[9] Scoville J.T. and La Haye R.J. 2003 *Nucl. Fusion* **43** 250
[10] Scoville J.T. 2006 Rotation of a neutral beamline to obtain counter-injection on the DIII-D tokamak *17th American Nuclear Society Topical Meeting on the Technology of Fusion Energy (Albuquerque, New Mexico, 2006)* 2007 *Fusion Sci. Technol.* at press
[11] Lohr J. *et al* 2005 *Fusion Sci. and Technol.* **48** 1226
[12] Anderson P.M., Hu Q., Murphy C.J., Reis E.E., Song Y. and Yao D. 2006 Design, fabrication and installation of the lower divertor for DIII-D *Proc. 24th Symp. on Fusion Technology (Warsaw, Poland, 2006)* 2007 *Fusion Eng. Des.* at press
[13] Penaflor B.G., Ferron J.R., Piglowski D.A., Johnson R.D., Baker D.R., Wade M.R. and Austin M.E. 2005 *Fusion Eng. Des.* **74** 659
[14] Humphreys D.A. *et al* 2007 Development of ITER-relevant plasma control solutions at DIII-D *Nucl. Fusion* **47** at press
[15] Holcomb C.T., Makowski M.A., Jayakumar R.J., Allen S.A., Ellis R.M., Geer R., Behne D., Morris K.L., Seppala L.G. and Moller J.M. 2006 *Rev. Sci. Instrum.* **77** 10E506
[16] Piglowski D.A., Ferron J.R., Gohil P., Johnson R.D. and Penaflor B.G. 2006 Enhancements in the second generation DIII-D digital plasma control system *Proc. 24th Symp. on Fusion Technology (Warsaw, Poland, 2006)* 2007 *Fusion Eng. Des.* at press
[17] Petty C.C., La Haye R.J., Luce T.C., Humphreys D.A., Hyatt A.W., Lohr J., Prater R., Strait E.J. and Wade M.R. 2004 *Nucl. Fusion* **44** 243
[18] Humphreys D.A., Ferron J.R., La Haye R.J., Luce T.C., Petty C.C., Prater R. and Welander A.S. 2006 *Phys. Plasmas* **13** 056113
[19] Prater R. *et al* 2007 Prevention of the 2/1 neoclassical tearing mode in DIII-D *Nucl. Fusion* **47** at press
[20] La Haye R.J., Humphreys D.A., Luce T.C., Ferron J.R., Perkins F.W., Petty C.C., Prater R., Strait E.J. and Welander A.S. 2004 Stabilization of neoclassical tearing modes by active control of electron cyclotron current drive alignment in DIII-D *Proc. 31st EPS Conf. on Plasma Physics (London, UK, 2004)* vol 28G (ECA) P-2.181
[21] Nagasaki K., Isayama A. and Ide S. 2003 *Nucl. Fusion* **43** L7
[22] Freidberg J.P. 1987 *Ideal Magnetohydrodynamics* (New York: Plenum Press)
[23] Strait E.J., Taylor T.S., Turnbull A.D., Ferron J.R., Lao L.L., Rice B., Sauter O., Thompson S.J. and Wróblewski D. 1994 *Phys. Rev. Lett.* **74** 2483
[24] Okabayashi M. *et al* 1996 *Nucl. Fusion* **36** 1167
[25] Sabbagh S.A. *et al* 2002 *Phys. Plasmas* **9** 2085
[26] Takeji S. *et al* 2002 *Nucl. Fusion* **42** 5
[27] Pinches S.D. *et al* 2003 MHD in JET advanced scenarios *Proc. 30th EPS Conf. on Plasma Physics (St Petersburg, Russia)* vol 27A P-1.93
[28] Garofalo A.M. *et al* 2002 *Phys. Plasmas* **9** 1997
[29] Sabbagh S.A. *et al* 2006 *Nucl. Fusion* **46** 635
[30] Matsunaga G. *et al* 2006 Stabilization effects of wall and plasma rotation on resistive wall mode in JT-60U *Proc. 33rd EPS Conf. on Plasma Physics (Rome, Italy, 2006)* vol 30I (ECA) O-2.003
[31] Okabayashi M. *et al* 2001 *Phys. Plasmas* **8** 2071
[32] Sabbagh S.A., Bell R.E., Menard J.E., Gates D.A., Sontag A.C., Bialek J.M., LeBlanc B.P., Levinton F.M., Tritz K. and Yuh H. 2006 *Phys. Rev. Lett.* **97** 045004
[33] Garofalo A.M., Strait E.J., Johnson L.C., La Haye R.J., Lazarus E.A., Navratil G.A., Okabayashi M., Scoville J.T., Taylor T.S. and Turnbull A.D. 2002 *Phys. Rev. Lett.* **89** 235001
[34] Reimerdes H. *et al* 2006 Reduced critical rotation for resistive wall mode stabilization in a near-axisymmetric configuration *Phys. Rev. Lett.* **98** 055001
[35] Solomon W.M., Burrell K.H., Andre R., Baylor L.R., Budny R., Gohil P., Groebner R.J., Holcomb C.T., Houlberg W.A. and Wade M.R. 2006 *Phys. Plasmas* **13** 056116
[36] Garofalo A.M. *et al* 2007 Active control of resistive wall modes in high beta, low rotation DIII-D plasmas *Nucl. Fusion* submitted
[37] Strait E.J. *et al* 2007 *Phys. Plasmas* **14** 056101
[38] Jensen T.H. 1993 *Phys. Fluids* B **5** 1239
[39] Fitzpatrick R. 1998 *Phys. Plasmas* **5** 3325
[40] Fitzpatrick R. 2002 *Phys. Plasmas* **9** 3459
[41] Liu Y.Q., Bondeson A., Fransson, C.M., Lennartson B. and Breitholtz C. 2000 *Phys. Plasmas* **7** 3681
[42] Evans T.E. *et al* 2004 *Phys. Rev. Lett.* **92** 235003
[43] Evans T.E. *et al* 2006 *Nature Phys.* **2** 419
[44] ITER Physics Basis Editors ITER Physics Expert Group Chairs and Co-Chairs, ITER Joint Central Team and Physics Integration Unit 1999 *Nucl. Fusion* **39** 2137

[45] Snyder P.B., Burrell K.H., Wilson H.R., Chu M.S., Fenstermacher M.E., Leonard A.W., Moyer R.A., Osborne T.H., Umansky M., West W.P. and Xu X.Q. 2007 Stability and dynamics of the edge pedestal in the low collisionality regime: physics mechanisms for steady-state ELM-free operation *Nucl. Fusion* submitted

[46] Osborne T.H., Snyder P.B., Burrell K.H., Evans T.E., Fenstermacher M.E., Leonard A.W., Moyer R.A., Schaffer M.J. and West W.P. 2006 Edge stability of stationary ELM-suppressed regimes on DIII-D *Phys. Plasmas* submitted

[47] Moyer R.A. *et al* 2006 Edge localized mode control in DIII-D using magnetic perturbation-induced pedestal transport changes *Proc. 21st Fusion Energy Conf. (Chengdu, China)* EX-9-3

[48] Burrell K.H. *et al* 1992 *Plasma Phys. Control. Fusion* **34** 1859

[49] Burrell K.H. *et al* 2002 *Plasma Phys. Control. Fusion* **44** A253

[50] Bécoulet M. *et al* 2006 Modeling of edge control by ergodic fields in DIII-D, JET, and ITER *Proc. 21st IAEA Fusion Energy Conf. (Chengdu, China)* IT/P1-29

[51] Whyte D.G. *et al* 2002 *Phys. Rev. Lett.* **89** 055001-1

[52] Hollmann E.M. *et al* 2005 *Nucl. Fusion* **45** 1046

[53] Rosenbluth M.N. and Putvinski S.V. 1997 *Nucl. Fusion* **37** 1355

[54] Luce T.C. *et al* 2006 Dependence of confinement and stability on variations in the external torque in the DIII-D tokamak *Proc. 21st Fusion Energy Conf. (Chengdu, China)* PD-3

[55] Wade M.R. *et al* 2005 *Nucl. Fusion* **45** 407

[56] Waltz R.E., Staebler G.M., Dorland W., Hammett G.W., Kostshenreuther M. and Konings J.A. 1997 *Phys. Plasmas* **4** 2482

[57] Staebler G.M., Kinsey, J.E. and Waltz R.E. 2006 A theory based transport model with comprehensive physics *Phys. Plasmas* submitted

[58] Carlstrom T.N., Groebner R.J., Fenzi C., McKee G.R., Moyer R.A. and Rhodes T.L. 2002 *Plasma Phys. Control. Fusion* **44** A333

[59] Ferron J.R., Gohil, P., Greenfield C.M., Lohr J., Luce T.C., Makowski M.A., Mazon D., Murakami M., Petty C.C., Politzer P.A. and Wade M.R. 2006 *Nucl. Fusion* **46** L13

[60] Wade M.R. *et al* 2003 *Nucl. Fusion* **43** 634

[61] Murakami M. *et al* 2005 *Nucl. Fusion* **45** 1419

[62] Yushmanov P.N. *et al* 1990 *Nucl. Fusion* **30** 1999

[63] Garofalo A.M. *et al* 2006 *Phys. Plasmas* **13** 056110

[64] Greenfield C.M. *et al* 1997 *Phys. Plasmas* **4** 1596

[65] West W.P. *et al* 2002 *Phys. Plasmas* **9** 1970

[66] Greenfield C.M. *et al* 2007 Progress toward high performance steady-state operation in DIII-D *Nucl. Fusion* submitted

[67] Ferron J.R. *et al* 2005 *Phys. Plasmas* **12** 056126

[68] Leonard A.W., Casper T.A., Groebner R.J., Osborne T.H., Snyder P.B. and Thomas D.M. 2007 Pedestal performance dependence upon plasma shape *Nucl. Fusion* submitted

[69] Luce T.C., Wade M.R., Ferron J.R., Hyatt A.W., Kellman A.G., Kinsey J.E., La Haye R.J., Lasnier C.J., Murakami M., Politzer P.A. and Scoville J.T. 2003 *Nucl. Fusion* **43** 321

[70] Mikkelsen D.R. 1989 *Phys. Fluids* B **1** 333

[71] Candy J. and Waltz R.E. 2003 *J. Comput. Phys.* **186** 545

[72] Politzer P.A. *et al* 2006 The dependence of the hybrid scenario on toroidal plasma rotation *Proc. 21st Fusion Energy Conf. (Chengdu, China)* EX-P1-9

[73] Chu M.S. *et al* 2007 Maintaining the quasi-steady state central current density profile in hybrid discharges *Nucl. Fusion* submitted

[74] Petrie T.W. *et al* 2006 A comparison of the radiating divertor in single- and double-null plasmas in DIII-D *Proc. 21st Fusion Energy Conf. (Chengdu, China)* EX-P1-16

[75] Wade M.R., Hogan J.T., Allen S.L., Brooks N.H., Hill D.N., Maingi R., Schaffer M.J., Watkins J.G., Whyte D.G., Wood R.D. and West W.P. 1998 *Nucl. Fusion* **38** 1839

[76] Nazikian R. *et al* 2006 *Phys. Rev. Lett.* **96** 105006

[77] Van Zeeland M.A., Kramer G.J., Austin M.E., Boivin R.L., Heidbrink W.W., Makowski M.A., McKee G.R., Nazikian R., Solomon W.M. and Wang G. 2006 *Phys. Rev. Lett.* **97** 135001

[78] Cheng C.Z. 1992 *Phys. Rep.* **1** 211

[79] Heidbrink W.W., Burrell K.H., Luo Y., Pablant N.A. and Ruskov E. 2004 *Plasma Phys. Control. Fusion* **46** 1855

[80] Rhodes T.L. *et al* 2006 ETG scale turbulence and transport in the DIII-D tokamak *Proc. 21st Fusion Energy Conf. (Chengdu, China)* EX/P4-37

[81] Rhodes T.L., Peebles W.A., Nguyen X., Van Zeeland M.A., deGrassie J.S., Doyle E.J., Wang G. and Zeng L. 2006 *Rev. Sci. Instrum.* **77** 10E922

[82] Kotschenreuther M., Rewoldt G. and Tang W.M. 1995 *Comput. Phys. Commun.* **88** 128

[83] Rhodes T.L. *et al* 2006 Response of multi-scale turbulence to electron cyclotron heating in the DIII-D tokamak *Phys. Plasmas* submitted

[84] Diamond P., Itoh S.-I., Itoh K. and Hahm T.S. 2005 *Plasma Phys. Control. Fusion* **47** R35

[85] McKee G.R., Fonck R.J., Gupta D.K., Schlossberg D.J., Shafer M.W. and Boivin R.L. 2006 *Rev. Sci. Instrum* **77** 10F104

[86] McKee G.R. *et al* 2007 Characterization of zonal flows and their dynamics in the DIII-D tokamak, laboratory plasmas, and simulation *Nucl. Fusion* submitted

[87] McKee G.R., Gupta D.K., Fonck R.J., Schlossberg D.J., Shafer M.W. and Gohil P. 2006 *Plasma Phys. Control. Fusion* **48** S123

[88] Holland C., Tynan G.R., Fonck R.J., McKee G.R. and Gupta D.K. 2006 Measurement of nonlinear interactions between geodesic acoustic modes and edge turbulence in the DIII-D tokamak *Phys. Rev. Lett.* submitted

[89] Gupta D.K., Fonck R.J., McKee G.R., Schlossberg D.J. and Shafer M.W. 2006 *Phys. Rev. Lett.* **97** 125002

[90] Austin M.E. *et al* 2006 *Phys. Plasmas* **13** 082502

[91] Koide Y. *et al* 1994 *Phys. Rev. Lett.* **72** 3662

[92] de Baar M.R., Beurskens N.A., Hogeweij M.D. and Lopes Cardozo N.J. 1999 *Phys. Plasmas* **6** 4645

[93] Bell M.G. *et al* 1999 *Plasma Phys. Control. Fusion* **41** A719

[94] Joffrin E. *et al* 2002 *Plasma Phys. Control Fusion* **44** 1739

[95] Waltz R.E., Austin M.E., Burrell K.H. and Candy J. 2006 *Phys. Plasmas* **13** 052301

[96] Wampler W., McLean A.G., Allen S.L., Brooks N.H., Elder J.D., Fenstermacher M.E., Groth M., Stangeby P.C., West W.P. and Whyte D.G. 2007 Transport and deposition of ^{13}C from methane injection into partially detached divertor H-mode plasmas in DIII-D *J. Nucl. Mater.* submitted

[97] Allen S.L. *et al* 2005 *J. Nucl. Mater.* **337–339** 30

[98] Elder J.D. *et al* 2005 *J. Nucl. Mater.* **337–339** 79

[99] Elder J.D. *et al* 2006 OEDGE modeling of the DIII-D H-mode $^{13}CH_4$ puffing experiment *Proc. 17th Plasma Surface Interactions in Controlled Fusion Devices (Hefei, People's Republic of China) J. Nucl. Mater.* submitted

[100] Stangeby P.C. *et al* 2006 Thermal oxidation experiments aimed at understanding tritium recovery based on ^{13}C-tracer experiments in DIII-D, JET, C-Mod, and MAST *Proc. 33rd EPS Conf. on Plasma Physics (Rome, Italy, 2006)* Paper P5.145 and http://eps2006.frascati.enea.it/papers/html/s_index.htm

[101] Krieger K. *et al* 2007 Formation of deuterium–carbon inventories in gaps of plasma facing components *J. Nucl. Mater.* submitted

[102] Rudakov D.L., Boedo J.A., Moyer R.A., Litnovsky A., Philipps V. 2006 *Rev. Sci. Instrum.* **77** 10F126

[103] Bray B.D., West W.P. and Rudakov D. 2007 Correlations of dust particles with plasma parameters in DIII-D *Proc. 21st Fusion Energy Conf. (Chengdu, China)* EX-P4-4

[104] West W.P., Bray B.D. and Burkart J. 2006 *Plasma Phys. Control. Fusion* **48** 1661
[105] Lipschultz B. *et al* 2006 *Phys. Plasmas* **13** 056117
[106] Maingi R., Jackson G.L., Wade M.R., Mahdavi M.A., Mioduszewski P.K., Haas G., Schaffer M.J., Hogan J.T. and Klepper C.C. 1996 *Nucl. Fusion* **36** 245
[107] Jackson G.L., Baker D.R., Holtrop K.L., Konoshima S., Maingi R., Staebler G.M. and West W.P. 1992 *J. Nucl. Mater.* **196–198** 236